SIRT1 attenuates blood-spinal cord barrier disruption after spinal cord injury by deacetylating p66Shc

Tao Jiang [a,1], Tao Qin [a,1], Peng Gao [a,1], Zhiwen Tao [a], Xiaowei Wang [a], Mengyuan Wu [a], Jun Gu [b], Bo Chu [b], Ziyang Zheng [a], Jiang Yi [a], Tao Xu [a], Yifan Huang [a], Hao Liu [a], Shujie Zhao [a,****], Yongxin Ren [a,***], Jian Chen [a,**], Guoyong Yin [a,*]

[a] *Department of Orthopedics, The First Affiliated Hospital of Nanjing Medical University, Nanjing, 210029, Jiangsu, China*
[b] *Department of Orthopedics, Xishan People's Hospital, Wuxi, 214000, Jiangsu, China*

ARTICLE INFO

ABSTRACT

Disruption of the blood-spinal cord barrier (BSCB) leads to inflammatory cell infiltration and neural cell death, thus, contributing to poor functional recovery after spinal cord injury (SCI). Previous studies have suggested that Sirtuin 1 (SIRT1), an NAD$^+$-dependent class III histone deacetylase, is abundantly expressed in endothelial cells and promotes endothelial homeostasis. However, the role of SIRT1 in BSCB function after SCI remains poorly defined. Here, we report that SIRT1 is highly expressed in spinal cord endothelial cells, and its expression significantly decreases after SCI. Using endothelial cell-specific SIRT1 knockout mice, we observed that endothelial cell-specific knockout of SIRT1 aggravated BSCB disruption, thus, resulting in widespread inflammation, neural cell death and poor functional recovery after SCI. In contrast, activation of SIRT1 by the agonist SRT1720 had beneficial effects. In vitro, knockdown of SIRT1 exacerbated IL-1β-induced endothelial barrier disruption in bEnd.3 cells, whereas overexpression of SIRT1 was protective. Using RNA-seq and IP/MS analysis, we identified p66Shc, a redox protein, as the potential target of SIRT1. Further studies demonstrated that SIRT1 interacts with and deacetylates p66Shc, thereby attenuating oxidative stress and protecting endothelial barrier function. Overall, our results indicate that SIRT1 decreases endothelial ROS production and attenuates BSCB disruption by deacetylating p66Shc after SCI, and suggest that SIRT1 activation has potential as a therapeutic approach to promote functional recovery against BSCB disruption following SCI.

1. Introduction

Spinal cord injury (SCI) usually leads to devastating motor and neurological disabilities [1]. Analogous to the function of the blood-brain barrier (BBB), the blood-spinal cord barrier (BSCB), composed of nonfenestrated endothelial cells, basement membrane, pericytes and astrocytic end foot processes, separates the parenchyma of the spinal cord from the peripheral circulation and is essential for maintaining internal environmental homeostasis in the spinal cord [2]. Mechanical forces during SCI directly damage spinal cord tissue, including the BSCB [3]. Disruption of the BSCB allows serum proteins, many of which are detrimental to neurons and glia, to enter the spinal cord, and also promotes infiltration of peripheral immune cells, which participate in the inflammatory response and release inflammatory factors, including tumor necrosis factor-α (TNF-α) and interleukin (IL)-1β. The inflammatory response in turn may further compromise BSCB integrity, thereby leading to irreversible functional disabilities [4]. Therefore, attenuating BSCB disruption should be considered a potential target for therapeutic intervention after SCI.

Unlike the peripheral circulation, highly evolved and complex tight junctions (TJs) are found between adjacent endothelial cells of the BBB/ BSCB, thus, severely restricting the paracellular permeability and

forming the structural basis of the BBB/BSCB [5,6]. TJs are composed of TJ proteins, including zonula occludens 1 (ZO-1), occludin and claudin5—transmembrane proteins whose expression is closely associated with BBB/BSCB permeability [7]. TJ proteins decrease in rodent models after SCI, thus compromising the integrity of the BSCB [3]. Moreover, strategies to prevent BSCB disruption by attenuating the degradation of TJ proteins can improve locomotor function after SCI [8].

Sirtuin 1 (SIRT1), the closest mammalian homolog of silent information regulator 2 (Sir2), is an NAD$^+$-dependent class III histone deacetylase [9,10]. Previous studies have shown that SIRT1 is abundantly expressed in endothelial cells, and regulates aging, inflammation, apoptosis and autophagy of endothelial cells by deacetylating histones and nonhistone proteins, thus playing important roles in diabetes, atherosclerosis, and other cardiovascular diseases [11] [–] [14]. Furthermore, increasing evidence suggests that decreased SIRT1 expression in cerebrovascular endothelial cells results in increased BBB permeability, which is associated with ischemic stroke, subarachnoid hemorrhage and Alzheimer's disease [15] [–] [17]. Moreover, the activation of SIRT1 by melatonin attenuates sepsis-induced BBB disruption [18]. However, the role of SIRT1 in the function of the BSCB and whether SIRT1 might promote functional recovery by attenuating BSCB disruption after SCI have not been elucidated.

In the present study, we examined the effects of SIRT1 on BSCB function, both in vivo and in vitro. We show that endothelial SIRT1 attenuates degradation of TJs and protects the BSCB, thus decreasing inflammatory cell infiltration and neural cell death, and promoting motor function recovery after SCI. We further demonstrate that the protective effect of SIRT1 is mediated at least partly by attenuation of oxidative stress through deacetylation of p66Shc. Our results reveal that targeting SIRT1 may be a promising treatment for SCI.

2. Materials and methods

2.1. Animals and treatments

All animal experiments were previously approved by the Animals Committee of Nanjing Medical University. The animals were cultivated under a 12-h-light-dark cycle at room temperature and given ad libitum access to food and water. SIRT1$^{flox/flox}$ and Tie2-Cre mice (C57BL/6J background) were both acquired from Cyagen Biosciences (Cyagen Biosciences, Guangzhou, China). Endothelial cell-specific knockout of SIRT1 was achieved by interbreeding SIRT1$^{flox/flox}$ mice with Tie2-Cre transgenic mice [19,20]. We crossed 8–10 week-old SIRT1$^{flox/flox}$ mice (control) and Tie2-Cre SIRT1$^{flox/flox}$ mice (SIRT1 CKO) for experiments. To investigate the effect of knockdown of endothelial SIRT1 on BSCB, mice were divided into two groups: SIRT1$^{flox/flox}$ mice group and SIRT1 CKO mice group (n = 6 animals per group for EB extravasation, Western blot, immunostaining and transmission electron microscopy, n = 12 animals per group for functional behavioral assessment). Wild-type C57BL/6J mice (8–10 weeks of age) were obtained from the Animal Center of Nanjing Medical University. SRT1720 (Selleck, USA), a selective SIRT1 agonist, was dissolved in 1% dimethyl sulfoxide (DMSO). The vehicle treatment comprised 1% DMSO. To investigate the effect of SRT1720 on BSCB, wild-type C57BL/6J mice were randomly divided into two groups: vehicle group and SRT1720 group (n = 6 animals per group for EB extravasation, Western blot, immunostaining and transmission electron microscopy, n = 12 animals per group for functional behavioral assessment). The wild-type C57BL/6J mice in the two group were intrathecally injected with 5 μL vehicle (vehicle group) or 1 μg/5 μL (50 μg/kg) SRT1720 (SRT1720 group) 1 h after SCI and for three consecutive days, as described previously.

2.2. SCI model

The SCI model was generated in 8–10 week-old mice, as described previously [21]. After the mice were anesthetized by isoflurane inhalation, laminectomy was performed to expose the spinal cord at T10. Subsequently, a spinal cord impactor (RWD, China) was used to induce SCI by dropping a rod (weighing 5 g) onto the spinal cord from a height of 6.5 cm. Sham-operated control mice underwent T10 laminectomy without SCI. After injury, the muscle layers and skin were sutured. The mice were placed on a warming blanket and maintained at 37 °C until they were fully awake. During recovery, mice were given antibiotics (penicillin, 32000 U/20 g) for 3 d, and their bladders were manually emptied twice daily until bladder function returned.

2.3. Endothelial cell isolation and flow cytometry

Isolation of vascular endothelial cells of the spinal cord was performed as described previously with some modifications [22]. The spinal cords of a group of five mice were used in each isolation. Briefly, after mice were sacrificed, a 10-mm length of T10 spinal cord segment containing the lesion site was removed and transferred to a 10-cm Petri dish filled with cold PBS on ice. The tissues were minced and incubated with collagenase/dispase for 45 min at 37 °C. Subsequently, myelin and debris were removed by centrifugation through Percoll. Cell pellets were resuspended and stained with PE/Cy7-labeled anti-CD31 (Thermo Fisher Scientific, USA) for 20 min at room temperature. Finally, CD31$^+$ endothelial cells were analyzed and sorted with a flow cytometer (Beckman Coulter, USA). Unstained controls were used to set up laser parameters and gating for samples. For RNA extraction, the sorted cells were immediately lysed for quantitative real-time PCR (qRT-PCR).

2.4. Evaluation of BSCB permeability

The permeability of the BSCB was examined with Evans blue (EB) dye extravasation, as described previously [23]. EB (2%, 0.2 ml; Aladdin, China) was administered via tail vein injection. One hour later, the mice were anesthetized and killed by intracardiac perfusion with saline and 4% paraformaldehyde (PFA). A 10-mm length of T10 spinal cord segment containing the lesion site was dissected and stored in 4% PFA. For qualitative examination of EB extravasation, the spinal cord tissues were cut into 14 μm thick transverse sections with a cryostat. The fluorescence of EB was observed with a fluorescence microscope (Leica, Germany) 1 mm caudal to the lesion epicenter in transverse sections, and the relative fluorescence intensity was quantitatively analyzed in ImageJ software (National Institutes of Health, USA).

The content of EB in the spinal cord tissues was quantified as described previously [24]. Briefly, the mice were killed and perfused with saline. A 10-mm length of T10 spinal cord segment containing the lesion site was extracted and weighed, then homogenized in 50% trichloroacetic acid solution. After centrifugation at $12,000 \times g$ for 20 min, supernatants were collected, and the fluorescence was measured with a spectrophotometer (BioTek, USA) at 620 nm excitation and 680 nm emission. EB content was quantified as μg dye/g tissue with a standard curve.

2.5. Functional behavioral assessment

All mice were acclimated to an open-field environment for 1 h before functional behavioral assessment (n = 12 animals per group). The data were collected by two trained investigators who were blinded to the experiment design. The ten-point (0–9) Basso Mouse Scale (BMS) score was used to assess the motor recovery of the injured mice. The test was performed before the surgical procedures and on days 1, 3, 7, 14, 21 and 28 after injury. Footprint analysis was performed as previously described [25]. The forelimbs and hindlimbs of the mice were painted with blue and red dyes, respectively, to record the walking pattern. The stride lengths and widths were examined and analyzed only when the mice ran at constant velocity.

2.6. Immunofluorescence staining

The mice were anesthetized and killed by intracardiac perfusion with saline and 4% PFA (n = 6 animals per group). A 10-mm length of T10 spinal cord segment containing the lesion site was dissected and fixed overnight in 4% PFA. The spinal cord samples were dehydrated in 20% and 30% sucrose solutions overnight. Subsequently, the frozen tissues were embedded in OCT and serially sectioned into 14 μm slices with a Leica CM1860 cryostat. For spinal cord immunofluorescence staining, the frozen sections were blocked with 5% goat serum for 1 h and incubated at 4 °C overnight with the following primary antibodies: anti-SIRT1 (1:200, Abcam), anti-CD31 (1:200, Santa Cruz Biotechnology; 1:200, BD), anti-GFAP (1:1000, Abcam), anti-F4/80 (1:200, Abcam), anti-NeuN (1:200, Abcam), anti-Olig2 (1:200, Abcam), anti-ZO-1 (1:200, Invitrogen), anti-claudin5 (1:200, Invitrogen) and anti-8-OHdG (1:200, bioss). On the next day, the slides were rinsed with PBS and incubated with secondary antibodies (Alexa Fluor 488, Alexa Fluor, 594; 1:200; Jackson ImmunoResearch) at room temperature for 1 h. After being rinsed with PBS, the sections were counterstained with DAPI. The images were captured with a fluorescence microscope (Leica, Germany).

2.7. Transmission electron microscopy

Transmission electron microscopy (TEM) was used to examine BSCB ultrastructure. Briefly, spinal cord tissues containing the lesion core were removed, cut into $1 \times 1 \times 1$ mm^3 blocks and fixed in 2.5% glutaraldehyde followed by 2% osmium tetroxide. After fixation, ultrathin sections were cut with a Leica ultramicrotome and placed on copper grids, then stained with uranyl acetate and lead citrate. The ultrastructures of vessel endothelium and tight junctions were examined with TEM (Hitachi HT7800).

2.8. Cell culture

Mouse brain microvascular endothelial cells (bEnd.3 cells) and HEK293T cells were obtained from the Type Culture Collection of the Chinese Academy of Sciences (Shanghai, China) and cultured in DMEM (Gibco, USA) supplemented with 10% FBS (Gibco, USA) and 1% penicillin-streptomycin (Gibco, USA). The incubator was set to 5% CO$_2$ at 37 °C. The bEnd.3 cells were passaged every 2–3 days until 80–90% confluence was reached.

2.9. Transepithelial electrical resistance measurement

Transepithelial electrical resistance (TEER) values were measured to reflect the integrity of the endothelial monolayer in vitro, as previously described [26]. The bEnd.3 cells were seeded into the upper "apical" chamber of Transwell inserts (Millipore, USA) and allowed to reach confluence. TEER values were measured with a Millicell ERS-Volt-Ohm Meter (Millipore, USA). The TEER values were normalized to the area of the culture inserts and are reported as Ω·cm^2.

2.10. Paracellular permeability measurement

The paracellular permeability was measured based on diffusion of FITC-dextran (70 kDa; Sigma Aldrich, USA) across the bEnd.3 cell monolayer, as previously described [27]. The bEnd.3 cells were seeded in the upper chambers of Transwell inserts (Millipore, USA) and allowed to reach confluence. Then FITC-dextran (1 mg/mL) was added to the upper chamber and incubated at 37 °C for 60 min. Subsequently, 100 μL of medium was collected from the basal chamber, and the fluorescence intensity was measured with a fluorescence spectrophotometer (BioTek, USA) at 485 nm (excitation) and 525 nm (emission) wavelengths.

2.11. RNA extraction and quantitative real-time PCR

Total RNA of cells or tissues was extracted with an E.Z.N.A. Total RNA Kit (Omega Bio-tek, USA) according to the manufacturer's protocol. Reverse transcription was performed with a Reverse Transcription kit (Vazyme, China). The resultant cDNA was diluted tenfold in distilled RNase Free dH2O and stored at −20 °C. Then qRT-PCR was performed on a Light Cycler 2.0 instrument with a ChamQ SYBR qPCR Master Mix Kit (Vazyme, China) with a Step One Plus Real-Time PCR Detection System (Applied Biosystems, USA). Relative expression of target mRNAs was normalized to GAPDH expression. Gene expression was quantified with a modification of the $2^{-\Delta\Delta Ct}$ method. The sequences of the primers used were as follows: SIRT1 forward 5′-TCGGCTACCGAGGTCCATA-3′ and reverse 5′-ACAATCTGCCACAGCGTCAT-3′; ZO-1 forward 5′-GATAGTTTGGCAGCAAGAGATGGTA-3′ and reverse 5′-AGGTCAGG-GACGTTCAGTAAGGTAG-3′; occludin forward 5′-CCTTCTGCTTCATC GCTTCCTTA-3′ and reverse 5′-CGTCGGGTTCACTCCCATTAT-3′; claudin5 forward 5′-AGTTAAGGCACGGGTAGCAC-3′ and reverse 5′-GTACTTCTGTGACACCGGCA-3′; and GAPDH forward 5′-TGAACGG-GAAGCTCACTGG-3′ and reverse 5′-GCTTCACCACCTTCTTGATGTC-3′.

2.12. Western blot assays

Total proteins of cells or tissues were extracted with RIPA lysis buffer (Beyotime, China) supplemented with PMSF. After centrifugation at $12000 \times g$ for 15 min at 4 °C, the supernatants were collected, and the protein concentration was quantified with a BCA protein assay kit (Beyotime, China). Equal amounts of proteins were separated with sodium dodecyl sulfate polyacrylamide gel electrophoresis gels and subsequently transferred to PVDF membranes. The membranes were then blocked in PBST containing 5% BSA for 1.5 h at room temperature, then incubated overnight at 4 °C with primary antibodies against ZO-1 (1:500, Invitrogen), occludin (1:1000, Proteintech), claudin5 (1:1000, Invitrogen), β-tubulin (1:1000, Proteintech), β-actin (1:1000, Abmart), p66Shc (1:1000, BD), p-p66Shc (1:1000, Santa Cruz), Ac-lysine (1:1000, Santa Cruz), p65 (1:1000, CST) and Ac-p65 (1:1000, Abcam). After washing with TBST and incubation with horseradish peroxidase (HRP)-conjugated corresponding secondary antibodies (1:10000, Proteintech) for 1 h, the protein bands were developed with enhanced chemiluminescence (ECL) detection reagents (Millipore, USA). The immunoreactive bands were visualized with a Tanon 4600SF System (Tanon, China), and the results were quantified in ImageJ software.

2.13. Transfection of siRNA and plasmids

All siRNAs were custom-synthesized by RiboBio Co., Ltd. (Guangzhou, China). The siRNA duplexes were dissolved in RNase-free water. bEnd.3 cells were transfected with 10 nM SIRT1 small interfering RNA (si-SIRT1), si-p66Shc or siRNA negative control (si-NC) for 48 h with Lipofectamine 2000 transfection reagent (Thermo Fisher Scientific, USA) according to the manufacturer's instructions. Specific silencing was confirmed by qRT-PCR and western blotting.

Full-length sequences for SIRT1 and p66Shc were cloned into the *Eco*RI and *Not*I sites of the Flag or His tagged pcDNA3.1 vector (Thermo Fisher Scientific, USA). qRT-PCR was used to clone cDNAs for SIRT1 (1–737 aa), SIRT1 N (1–250 aa), SIRT1 ΔC (1–480 aa), SIRT1 ΔN (223–737 aa), p66Shc (1–579 aa), p66Shc (1–155 aa), p66Shc (156–579 aa), p66Shc (340–579 aa) and p66ShcK81R into the corresponding vectors. bEnd.3 cells or HEK293T cells were transfected with Lipofectamine 2000 reagent (Thermo Fisher Scientific, USA) according to the manufacturer's instructions.

2.14. Immunoprecipitation

The cells were rinsed with ice-cold PBS and lysed for 30 min in immunoprecipitation (IP) lysis buffer (Beyotime, China) at 4 °C. After

centrifugation at 12,000×*g* for 20 min, the supernatant was extracted, then incubated with the indicated antibodies and Protein A/G magnetic beads (Thermo Fisher Scientific, USA) at 4 °C overnight with slow rotation. After conjugation, the beads were washed with ice-cold IP-lysis buffer three times. Subsequently, input and immunoprecipitates were subjected to western blotting.

2.15. Immunoprecipitation coupled with mass spectrometry

Whole cell protein lysates were extracted from bEnd.3 cells after treatment with 10 ng/ml IL-1β for 24 h, and IP was performed with the indicated antibodies and Protein A/G magnetic beads (Thermo Fisher Scientific, USA), as described above. The extracted immunoprecipitates were evaluated with an Easy-nLC 1000 mass spectrometer (Thermo Fisher Scientific, USA).

2.16. Detection of intracellular ROS, mitochondrial ROS and mitochondrial membrane potential

The intracellular reactive oxygen species (ROS) levels in bEnd.3 cells were detected via 2′,7′-dichlorofluorsecein-diacetate (DCFH-DA) with a ROS Assay Kit (Beyotime, China) according to the manufacturer's instructions. Cell fluorescence was measured with flow cytometry (Beckman Coulter, USA). Data were analyzed in FlowJo software (Version 10.6.1). Mitochondrial ROS were detected with MitoSOX™ Red Mitochondrial Superoxide Indicator (Invitrogen, USA) according to the manufacturer's instructions. The cells were observed under a confocal microscope (Leica, Germany). The mitochondrial membrane potential was detected with a JC-1 Assay Kit (Beyotime, China) followed by flow cytometry analysis according to the manufacturer's instructions. The aggregate-to-monomer (red/green) fluorescence intensity ratio was used to quantify the mitochondrial potential.

2.17. Statistical analyses

Data are presented as the mean ± standard deviation. All experiments were performed at least three times. Statistical analyses ware performed in GraphPad Prism 7.0 (GraphPad Software Inc., USA). Unpaired two-tailed Student's t-tests were used for analyses of two groups, and ANOVA followed by the Tukey's post hoc test was used for analyses of more than two groups. A value of P < 0.05 was considered statistically significant.

3. Results

3.1. BSCB is disrupted after SCI

To systematically examine the changes in BSCB integrity, we generated contusion SCI in wild-type C57BL/6J mice, then visualized BSCB permeability through EB extravasation at 8 h, 1 d, 3 d, 7 d and 14 d after SCI. As shown in Fig. 1A, the EB extravasation significantly increased as early as 8 h after injury and returned to nearly normal by 14 days postinjury. Similarly, the fluorescence intensity of EB indicated that the BSCB permeability significantly increased at 8 h after SCI, peaked at 1 d, and was nearly restored by 14 d (Fig. 1B and C), thereby indicating the disruption of the BSCB after SCI, and nearly re-established BSCB function at 14 days postinjury. Quantification of EB content in clarified spinal cord lysates validated the results (Fig. 1D). Disruption of the BSCB is known to be associated with degradation and decreased expression of endothelial TJ proteins after SCI. We then performed western blotting to examine the expression of TJ proteins (ZO-1, occludin and claudin5), which are required for normal BSCB integrity. The expression of TJ proteins was significantly lower in mice after SCI than in sham-operated control mice (Fig. 1E–H), thus indicating that TJs were compromised after SCI. Together, these results indicated that the BSCB is disrupted in early stages of SCI and is subsequently re-established.

3.2. SIRT1 expression decreases in spinal cord endothelial cells after SCI in vivo

Next, we used qRT-PCR and western blotting to examine the expression of SIRT1 in the spinal cord in wild-type C57BL/6J mice at different stages after SCI. Compared with sham-operated mice, SIRT1
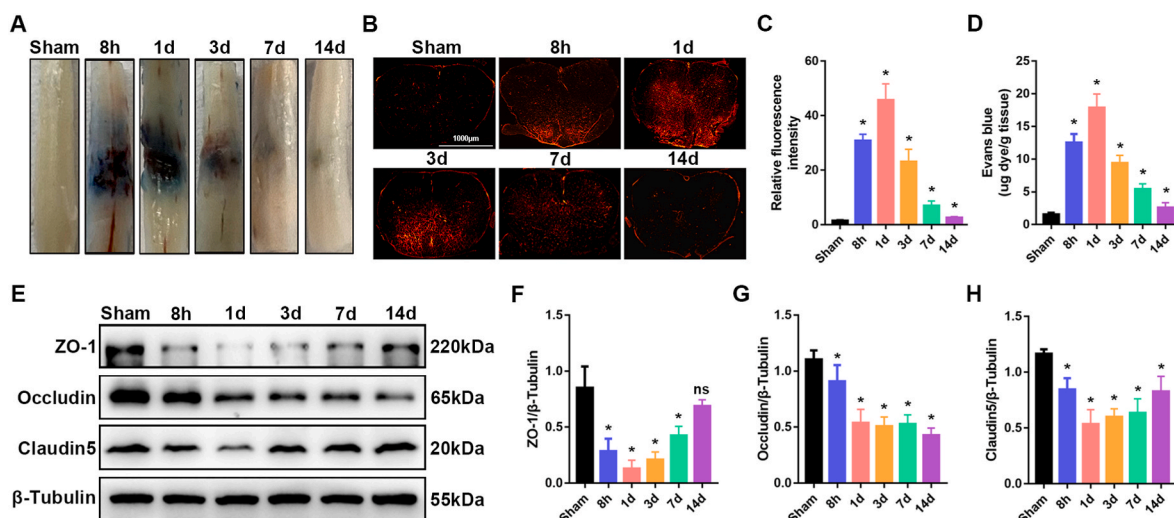
Fig. 1. The BSCB is disrupted, and TJ protein expression is decreased after SCI. For evaluation of BSCB permeability, 2% Evans blue dye was intravenously injected via the tail vein. (**A**) Representative images of spinal cords, showing EB extravasation in sham-operated mice, and at 8 h, 1 d, 3 d, 7 d and 14 d after SCI in mice (n = 6 animals per group). (**B**) Immunofluorescence images of EB extravasation at a position 1 mm caudal to the lesion epicenter in the transverse sections of the spinal cord in sham-operated mice, and at 8 h, 1 d, 3 d, 7 d and 14 d after SCI in mice (n = 6 animals per group). (**C**) Quantification of EB fluorescence intensity for each group (n = 6 animals per group). (**D**) A 10-mm length of spinal cord containing the lesion site was extracted. Quantification of EB content by spectrophotometry in sham-operated mice, and at 8 h, 1 d, 3 d, 7 d and 14 d after SCI in mice (n = 6 animals per group). (**E**) Representative immunoblots of the TJ proteins ZO-1, occludin and claudin5 in the spinal cord in sham-operated mice, and at 8 h, 1 d, 3 d, 7 d and 14 d after SCI in mice (n = 6 animals per group). (**F–H**) Quantification of the expression of TJ proteins (n = 6 animals per group). *P < 0.05; ns, not significant; compared with the sham-operated group. (For interpretation of the references to colour in this figure legend, the reader is referred to the Web version of this article.)

mRNA expression and protein levels significantly decreased in early stages of SCI, then were gradually restored (Fig. 2A–C). The decreased expression of SIRT1 was roughly consistent with the disruption of the BSCB after SCI, thereby suggesting that SIRT1 may be involved in SCI-induced BSCB disruption. Previous studies have shown that SIRT1 is highly expressed in endothelial cells [12]. According to the brainrnaseq.org online database, SIRT1 may be highly expressed in endothelial cells of the spinal cord (Fig. S1A). We then performed immunofluorescence to examine the expression of SIRT1 in endothelial cells (CD31$^+$) and other spinal cord cell types, including astrocytes (GFAP+), neurons (NeuN+), oligodendrocytes (Olig2+) and microglia (Iba1+). Immunofluorescence indicated that SIRT1 was expressed mainly in endothelial cells and neurons, but not astrocytes, oligodendrocytes and microglia (Fig. 2D). These results demonstrated that SIRT1 is highly expressed in endothelial cells of the spinal cord, which are major components of the BSCB.

We then examined the change in SIRT1 in spinal cord endothelial cells after SCI. Co-immunostaining of SIRT1 with CD31$^+$ indicated that the expression of SIRT1 was significantly lower in endothelial cells in mice at 3 d after SCI than in sham-operated mice (Fig. 2E and F). To further validate the decreased expression of SIRT1 in endothelial cells of the spinal cord after SCI, we used flow cytometry to isolate endothelial cells of the spinal cord, then extracted RNA (Figs. S1B and C). qRT-PCR confirmed that SIRT1 expression significantly decreased in endothelial cells at 3 d after SCI (Fig. 2G). Together, these results suggested that SIRT1 expression significantly decreases in endothelial cells of the spinal cord after SCI, thus indicating that SIRT1 may play a crucial role in BSCB function after SCI.

3.3. Knockout of endothelial SIRT1 exacerbates disruption of the BSCB and impairs functional recovery after SCI

To investigate the role of SIRT1 in the BSCB after SCI in vivo, we crossed Tie2-Cre mice with SIRT1$^{flox/flox}$ mice to specifically delete SIRT1 in endothelial cells (Tie2-Cre:SIRT1$^{flox/flox}$, denoted SIRT1 KO mice hereafter) (Fig. S2A). Western blotting indicated that SIRT1 was successfully knocked out in the spinal cords and brain regions, including the cortex and cerebellum (Fig. S2B). Immunofluorescence further demonstrated that SIRT1 was knocked out in the endothelial cells of the spinal cord (Fig. S2C). No significant difference in body weight was observed between SIRT1$^{fl/fl}$ and SIRT1 CKO mice (Fig. S2D). BSCB integrity was normal in both SIRT1$^{fl/fl}$ and SIRT1 CKO mice without SCI (Figs. S2E and F). Moreover, no significant difference was observed in the density of blood vessels in spinal cords between SIRT1$^{fl/fl}$ and SIRT1 CKO mice (Figs. S2G and H). Both SIRT1$^{fl/fl}$ and SIRT1 CKO mice showed maximum BMS scores of 9 (Fig. S2I). Footprint analysis also demonstrated that the motor functions were normal in both SIRT1$^{fl/fl}$ and SIRT1 CKO mice (Fig. S2J-L). Collectively, these results demonstrated that SIRT1 knockout in endothelial cells did not alter the normal development of microvasculature in the spinal cord or motor function in mice without SCI.

EB extravasation was significantly greater in SIRT1 CKO mice at 3 d after SCI than in SIRT1$^{fl/fl}$ mice, thus indicating that knockout of endothelial SIRT1 exacerbated BSCB disruption after SCI in vivo (Fig. 3A–D). The SIRT1 CKO mice showed significantly greater secondary hemorrhage than SIRT1$^{fl/fl}$ mice, on the basis of examination of homogenates of injured spinal cord tissues (Fig. 3E). Co-immunostaining of ZO-1 with CD31 indicated that the fluorescence intensity of vascular ZO-1 was significantly diminished in SIRT1 CKO mice (Fig. 3F and G). Western blotting further demonstrated that the expression of TJ proteins was markedly lower in SIRT1 CKO mice than SIRT1$^{fl/fl}$ mice (Fig. 3H). TEM showed that the gap of TJs between two endothelial cells was more apparent, and the length of TJs was shorter, in SIRT1 CKO mice than SIRT1$^{fl/fl}$ mice (Fig. 3I–K), thus confirming that knockout of endothelial SIRT1 exacerbated damage to TJs and BSCB. These results indicated that
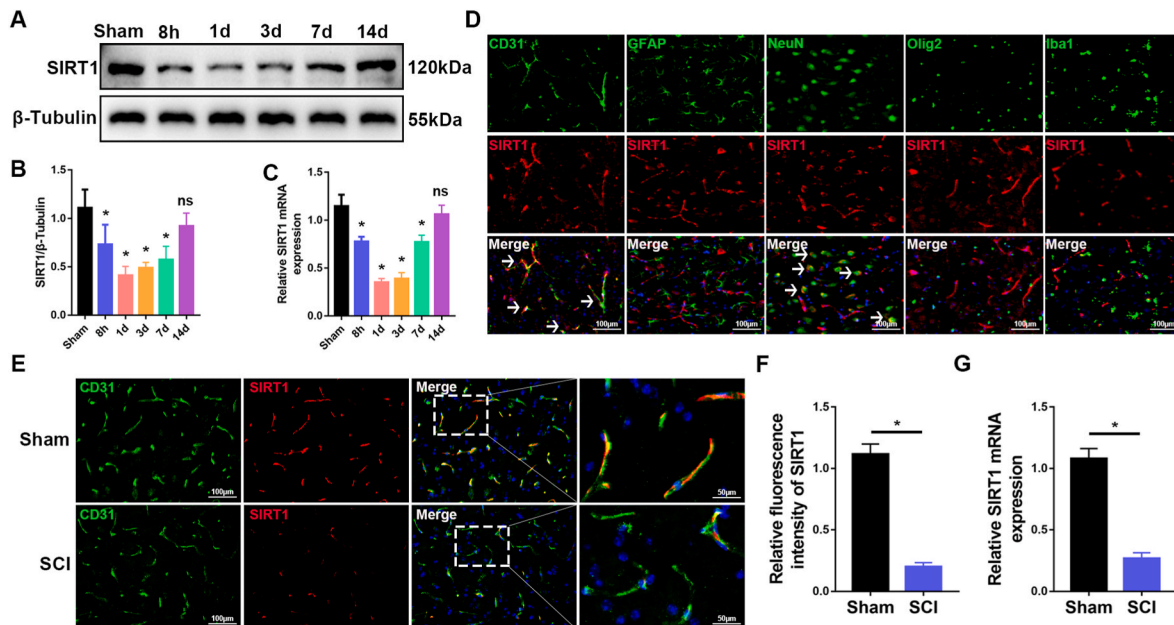
Fig. 2. SIRT1 expression decreases in endothelial cells of the spinal cord after SCI. (**A**) Western blot analysis of SIRT1 expression in the spinal cord in sham-operated mice, and at 8 h, 1 d, 3 d, 7 d and 14 d after SCI in mice (n = 6 animals per group). (**B**) Quantification of relative levels of SIRT1 protein (n = 6 animals per group). (**C**) qRT-PCR analysis of the mRNA level of SIRT1 in the spinal cord in sham-operated mice, and at 8 h, 1 d, 3 d, 7 d and 14 d after SCI in mice (n = 6 animals per group). (**D**) Double immunostaining images of spinal cord sections, showing that SIRT1 is expressed mainly in endothelial cells (CD31$^+$, white arrows) and neurons (NeuN+, white arrows), but is not expressed in astrocytes (GFAP+), oligodendrocytes (Olig2+) and microglia (Iba1+). (**E**) Representative immunofluorescence images of SIRT1 (red) and CD31$^+$ (green), showing lower SIRT1 expression in endothelial cells of the spinal cord in mice at 3 d after SCI than in sham-operated mice (n = 6 animals per group). (**F**) Quantification of SIRT1 expression (n = 6 animals per group). (**G**) qRT-PCR analysis of the mRNA level of SIRT1 in isolated endothelial cells of the spinal cord, showing lower SIRT1 expression in endothelial cells of the spinal cord in mice at 3 d after SCI than in sham-operated mice (n = 3 independent experiments). *P < 0.05; ns, not significant; compared with the sham-operated group. (For interpretation of the references to colour in this figure legend, the reader is referred to the Web version of this article.)
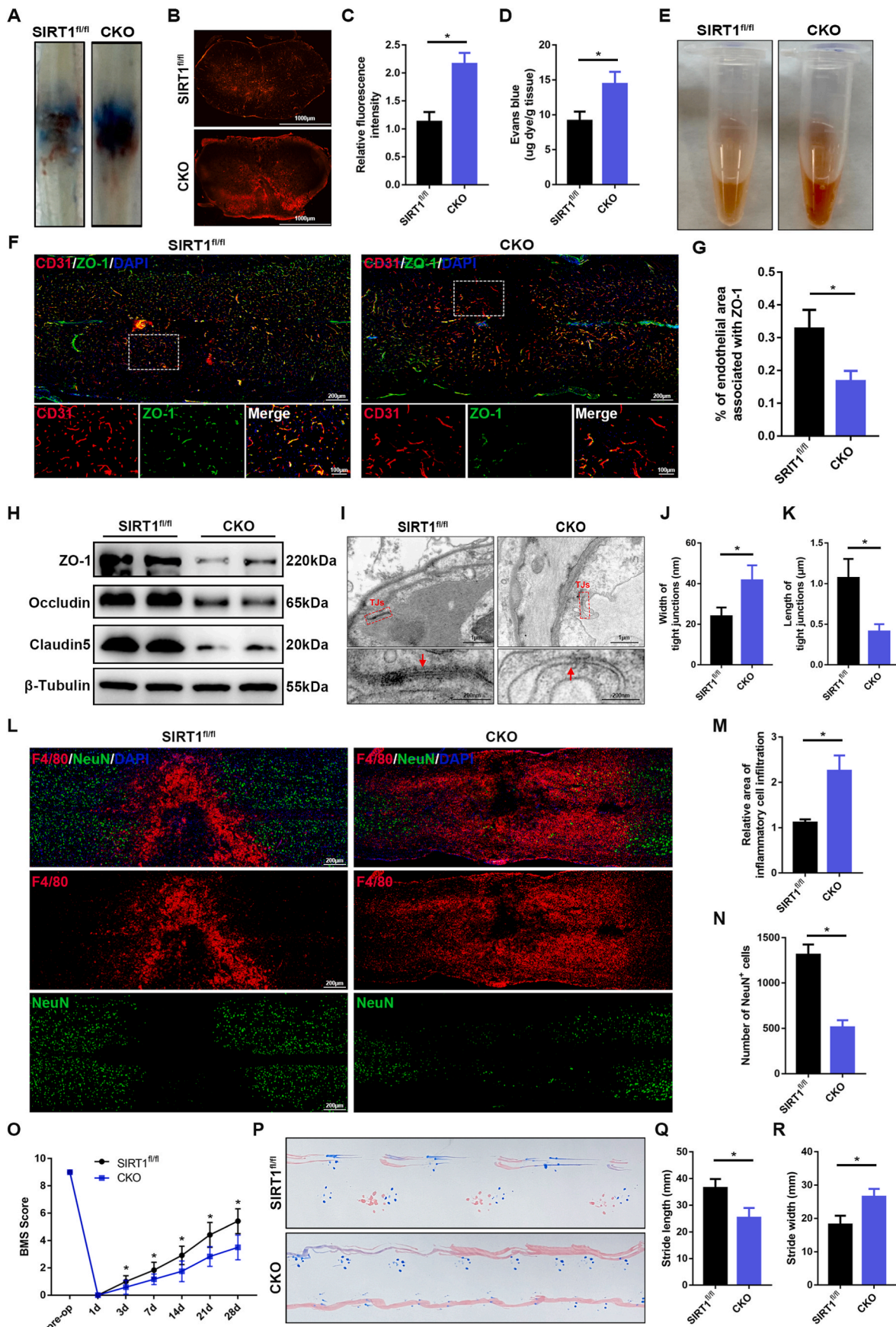
(caption on next page)

Fig. 3. Knockout of endothelial SIRT1 exacerbates disruption of the BSCB and impairs functional recovery after SCI. (**A**) Representative images of the spinal cord, showing EB extravasation at 3 d after SCI in SIRT1$^{fl/fl}$ and SIRT1 CKO mice (n = 6 animals per group). The spinal cords showed significantly greater EB extravasation in SIRT1 CKO mice than SIRT1$^{fl/fl}$ mice at 3 d after SCI. (**B**) Immunofluorescence images of EB extravasation 1 mm caudal to the lesion epicenter in the transverse sections of the spinal cord at 3 d after SCI in SIRT1$^{fl/fl}$ and SIRT1 CKO mice (n = 6 animals per group). (**C**) Quantification of EB fluorescence intensity for each group (n = 6 animals per group). (**D**) Quantification of EB content by spectrophotometry in the spinal cord at 3 d after SCI in SIRT1$^{fl/fl}$ and SIRT1 CKO mice (n = 6 animals per group). (**E**) Representative images of homogenized spinal cords, showing tissue blood at 3 d after SCI in SIRT1$^{fl/fl}$ and SIRT1 CKO mice (n = 6 animals per group). (**F**) Representative immunofluorescence images of ZO-1 (green) and CD31 (red) in the spinal cord at 3 d after SCI in SIRT1$^{fl/fl}$ and SIRT1 CKO mice (n = 6 animals per group). Images of selected regions are shown at higher magnification. Sections from SIRT1 CKO mice showed significantly lower endothelial ZO-1 expression than those from SIRT1$^{fl/fl}$ mice at 3 d after SCI. (**G**) Quantification of endothelial ZO-1 expression (n = 6 animals per group). (**H**) Representative immunoblots of the TJ proteins ZO-1, occludin and claudin5 in the spinal cord at 3 d after SCI in SIRT1$^{fl/fl}$ and SIRT1 CKO mice (n = 6 animals per group). (**I**) Representative TEM images of TJ ultrastructure in the spinal cord at 3 d after SCI in SIRT1$^{fl/fl}$ and SIRT1 CKO mice. Images of selected regions are shown at higher magnification. Red squares and red arrows indicate the TJs (n = 6 animals per group). (**J, K**) Quantification of the width and length of TJs (n = 6 animals per group). (**L**) Representative immunofluorescence images of NeuN (green) and F4/80 (red) in the spinal cord at 7 d after SCI in SIRT1$^{fl/fl}$ and SIRT1 CKO mice (n = 6 animals per group). The sections from SIRT1 CKO mice showed significantly greater inflammatory cell infiltration and fewer neurons than those from SIRT1$^{fl/fl}$ mice at 7 d after SCI. (**M**) Quantification of the area of F4/80$^+$ inflammatory cells (n = 6 animals per group). (**N**) Quantification of the number of NeuN$^+$ neurons (n = 6 animals per group). (**O**) BMS scores during 28 days of recovery after SCI in SIRT1$^{fl/fl}$ and SIRT1 CKO mice (n = 12 animals per group). SIRT1 CKO mice showed significantly poorer behavioral recovery than SIRT1$^{fl/fl}$ mice over the course of 28 days after SCI. (**P**) Representative images of footprint analysis at 28 d after SCI in SIRT1$^{fl/fl}$ and SIRT1 CKO mice (n = 12 animals per group). (**Q, R**) Quantification analysis of stride length and width (n = 12 animals per group). *P < 0.05 compared with the SIRT1$^{fl/fl}$ group. (For interpretation of the references to colour in this figure legend, the reader is referred to the Web version of this article.)

the knockout of SIRT1 in endothelial cells of the spinal cord resulted in greater BSCB vulnerability to pathological conditions after SCI.

SCI-induced BSCB disruption has been found to increase inflammatory cell infiltration, thus contributing to subsequent neural cell death and permanent neurological disability [28]. Immunostaining of F4/80 (a macrophage marker) showed significantly elevated inflammatory cell infiltration in SIRT1 CKO mice at 7 d after SCI (Fig. 3L and M). To assess neural cell death, we used NeuN to label neurons and examine the number of neurons around the lesion core. As shown in Fig. 3L, N, significantly fewer neurons were observed around the lesion core in SIRT1 CKO mice than SIRT1$^{fl/fl}$ mice at 7 d after SCI. To assess behavioral function after SCI, we performed several behavioral tests, including BMS scoring and footprint analysis. SIRT1 CKO mice showed significantly poorer behavioral recovery, in terms of walking, hindlimb movement and hind paw placement, than SIRT1$^{fl/fl}$ mice over the course of 4 weeks after SCI, as quantified by the BMS scores (Fig. 3O). Similarly, footprint analysis also indicated that SIRT1 CKO mice had poorer gait recovery and more limited motor coordination than SIRT1$^{fl/fl}$ mice (Fig. 3P–R). Together, these results demonstrated that endothelial cell-specific knockout of SIRT1 aggravates BSCB disruption, thus resulting in inflammatory cell infiltration, neural cell death and poor functional recovery in mice after SCI.

3.4. Activation of SIRT1 protects the BSCB and promotes functional recovery after SCI

To further examine the effects of SIRT1 on the BSCB after SCI, we performed intrathecal injection of SRT1720, a selective agonist of SIRT1, to activate SIRT1 in the spinal cord after SCI. As shown in Fig. 4A–E, treatment with SRT1720, compared with vehicle alone, significantly alleviated the EB extravasation and hemorrhage. Furthermore, immunofluorescence and western blotting demonstrated that treatment with SRT1720 attenuated the loss of TJ proteins after SCI (Fig. 4F–H). TEM further confirmed that treatment with SRT1720 preserved TJs after SCI (Fig. 4I–K). Treatment with SRT1720 also decreased inflammatory cell infiltration and neural cell death, thus significantly improving behavioral function after SCI (Fig. 4L–R). These results suggested that activation of SIRT1 by intrathecal injection of SRT1720 protects the BSCB and promotes functional recovery in vivo after SCI, thus, confirming a critical role of SIRT1 in protecting the function of the BSCB.

3.5. SIRT1 attenuates IL-1β-induced disruption of the BSCB in vitro

SCI provokes an inflammatory response that results in further tissue damage, including disruption of the BSCB [29]. The proinflammatory cytokines IL-1β and TNFα were up-regulated immediately after SCI

(Fig. S3). Among many proinflammatory cytokines, IL-1β is a key instigator mediating neuroinflammation after SCI; this cytokine is secreted mainly by microglia, astrocytes and blood-derived inflammatory cells after SCI. To further examine the role of SIRT1 in the BSCB, we treated monolayers of bEnd.3 cells (an immortalized mouse brain endothelial cell line) in vitro with IL-1β, as previously described [30]. Western blotting and qRT-PCR showed that the expression of SIRT1 and TJ proteins significantly decreased in a dose-dependent manner after treatment with IL-1β (0–50 ng/ml) for 24 h (Figs. S4A–I). Moreover, TEER assays and diffusion of FITC-dextran assays were used to evaluate the paracellular permeability in vitro. Treatment with IL-1β significantly decreased the TEER values and increased permeability to FITC-dextran in bEnd.3 cells (Figs. S4J and K). These results suggested that IL-1β decreases SIRT1 expression and disrupts the endothelial barrier in vitro. A dose of 10 ng/ml was chosen for subsequent experiments.

Next, bEnd.3 cells were transfected with si-SIRT1 or SIRT1 over-expression plasmid (SIRT1). qRT-PCR and western blotting confirmed the success of transfection (Figs. S5A–F). With TEER assays and diffusion of FITC-dextran assays, we demonstrated that knockdown of SIRT1 exacerbated the IL-1β-induced disruption of endothelial permeability (Fig. 5A and B). Western blotting indicated that knockdown of SIRT1 resulted in significantly lower expression of TJ proteins than that in the control group (Fig. 5C). Immunofluorescence staining also confirmed that knockdown of SIRT1 significantly decreased the expression of ZO-1 and claudin5 (Fig. 5D–F). In contrast, overexpression of SIRT1 attenuated IL-1β-induced endothelial hyperpermeability (Fig. 5G and H). Western blotting and immunofluorescence staining further demonstrated that the decrease in TJ proteins after IL-1β treatment was significantly rescued by overexpression of SIRT1 (Fig. 5I-L). Together, these results suggested that SIRT1 attenuates IL-1β-induced endothelial barrier disruption in vitro and consequently may have a potential role in the maintenance of BSCB function after SCI.

3.6. Endothelial SIRT1 attenuates oxidative stress

To determine the mechanism through which SIRT1 regulates BSCB function, we performed transcriptomic analysis via high-throughput RNA sequencing (RNA-Seq) on three biological replicates of bEnd.3 cells transfected with control vector or SIRT1-overexpression plasmid after IL-1β treatment (Fig. 6A). The differentially expressed genes (DEGs) in this study were defined as genes with fold changes >2 and p < 0.05. As shown in Fig. 6B via a volcano plot, 613 DEGs were upregulated and 456 DEGs were downregulated in the SIRT1 group compared with the vector group. As expected, GO analysis based on DEGs indicated that SIRT1 was associated with increased expression of some DEGs associated with cell-cell junctions and tight junctions (Fig. 6C), thus, indicating that upregulation of SIRT1 is beneficial to endothelial barrier
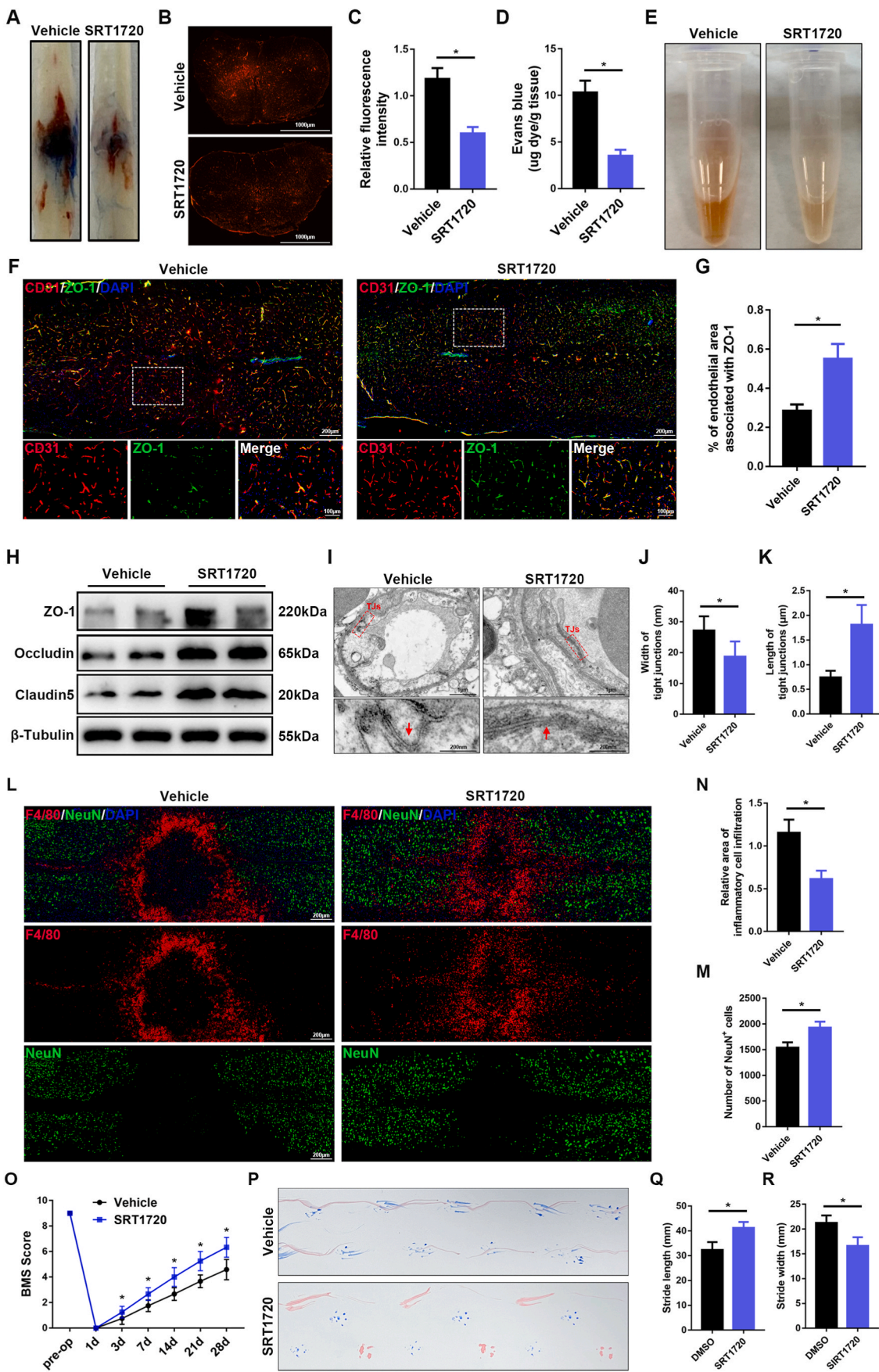
(caption on next page)

Fig. 4. Activation of SIRT1 protects the BSCB and promotes functional recovery after SCI. Vehicle or SRT1720 (50 μg/kg) was intrathecally injected into wild-type C57BL/6J mice 1 h after SCI and continued for 3 consecutive days. **(A)** Representative images of spinal cords, showing EB extravasation at 3 d after SCI in mice treated with vehicle or SRT1720 (n = 6 animals per group). The spinal cords from the mice treated with SRT1720, compared with vehicle, showed significantly less EB extravasation 3 d after SCI. **(B)** Immunofluorescence images of EB extravasation 1 mm caudal to the lesion epicenter in the transverse sections of the spinal cord at 3 d after SCI in mice treated with vehicle or SRT1720 (n = 6 animals per group). **(C)** Quantification of EB fluorescence intensity for each group (n = 6 animals per group). **(D)** Quantification of EB content by spectrophotometry in the spinal cord at 3 d after SCI in mice treated with vehicle or SRT1720 (n = 6 animals per group). **(E)** Representative images of homogenized spinal cords, showing tissue blood at 3 d after SCI in mice treated with vehicle or SRT1720 (n = 6 animals per group). **(F)** Representative immunofluorescence images of ZO-1 (green) and CD31 (red) in the spinal cord at 3 d after SCI in mice treated with vehicle or SRT1720 (n = 6 animals per group). Images of selected regions are shown at higher magnification. The sections from mice treated with SRT1720 compared with vehicle control showed significantly greater endothelial ZO-1 expression at 3 d after SCI. **(G)** Quantification of endothelial ZO-1 expression (n = 6 animals per group). **(H)** Representative immunoblots of the TJ proteins ZO-1, occludin and claudin5 in the spinal cord at 3 d after SCI in mice treated with vehicle or SRT1720 (n = 6 animals per group). **(I)** Representative TEM images of TJ ultrastructure in the spinal cord at 3 d after SCI in mice treated with vehicle or SRT1720. Images of selected regions are shown at higher magnification. Red squares and red arrows indicate the TJs (n = 6 animals per group). **(J, K)** Quantification of the width and length of TJs (n = 6 animals per group). **(L)** Representative immunofluorescence images of NeuN (green) and F4/80 (red) in the spinal cord at 7 d after SCI in mice treated with vehicle or SRT1720 (n = 6 animals per group). The sections from the mice treated with SRT1720, compared with vehicle control, showed significantly less inflammatory cell infiltration and more neurons at 7 d after SCI. **(M)** Quantification of the area of F4/80$^+$ inflammatory cells (n = 6 animals per group). **(N)** Quantification of the number of NeuN$^+$ neurons (n = 6 animals per group). **(O)** BMS scores during 28 days of recovery after SCI in mice treated with vehicle or SRT1720 (n = 12 animals per group). The mice treated with SRT1720, compared with vehicle control, showed better behavioral recovery over the course of 28 days after SCI. **(P)** Representative images of footprint analysis at 28 d after SCI in mice treated with vehicle or SRT1720 (n = 12 animals per group). **(Q, R)** Quantification analysis of stride length and width (n = 12 animals per group). *$P < 0.05$ compared with the vehicle control group. (For interpretation of the references to colour in this figure legend, the reader is referred to the Web version of this article.)

function. We also found that leukocyte chemotaxis, oxidative stress, regulation of ROS, and inflammatory responses were involved (Fig. 6C). Oxidative stress is caused by an imbalance between oxidants and anti-oxidants, thereby leading to excessive production of intracellular and mitochondrial ROS; this response has been demonstrated to be a major mechanism contributing to BBB/BSCB disruption [31]. As shown in Figs. S6A–F, the IL-1β-induced disruption of endothelial permeability and loss of TJ proteins was ameliorated by treatment with N-ace-tyl-cysteine (NAC), a ROS scavenger, thus, suggesting the critical role of ROS in endothelial barrier disruption, as previously reported.

We then examined whether SIRT1 might regulate oxidative stress in endothelial cells of the spinal cord after SCI. Immunofluorescence staining of 8-OHdG was performed to detect endothelial oxidative stress in vivo after SCI. Endothelial 8-OHdG was significantly higher in SIRT1 CKO mice than SIRT1$^{fl/fl}$ mice (Fig. 6D and E), whereas intrathecal in-jection of SRT1720 attenuated endothelial oxidative stress (Fig. 6 L, M), thus, indicating that SIRT1 decreased oxidative stress in the endothelial cells of the spinal cord after SCI. We further examined the effect of SIRT1 on oxidative stress in bEnd.3 cells in vitro. Treatment with IL-1β increased the production of intracellular ROS (as detected with DCFH-DA) and mitochondrial ROS (as detected with MitoSOX Red). Knock-down of SIRT1 significantly aggravated these effects (Fig. 6F–I), whereas overexpression of SIRT1 reversed them (Fig. 6N–Q). We also evaluated mitochondrial function with JC-1. Treatment with IL-1β decreased the mitochondrial potential of bEnd.3 cells, and knockdown of SIRT1 further aggravated the effect (Fig. 6J and K), whereas SIRT1 over-expression restored the mitochondrial potential (Fig. 6R and S). Together, these results revealed that endothelial SIRT1 attenuates oxidative stress, thereby protecting BSCB function after SCI.

3.7. SIRT1 interacts with p66Shc

To further investigate the mechanism underlying the regulation of BSCB function by SIRT1, we used IP coupled with mass spectrometry (IP/MS) to identify which proteins bind SIRT1. IP/MS identified p66Shc as a putative SIRT1 interacting protein (Fig. S7). Interestingly, p66Shc is a major regulator of ROS, in agreement with the above results indicating that SIRT1 regulates oxidative stress. Next, we performed co-IP analysis to confirm the IP/MS results. As shown in Fig. 7A, IP of endogenous SIRT1 co-precipitated p66Shc in bEnd.3 cells treated with IL-1β. The reverse experiment also confirmed that SIRT1 was precipitated by p66Shc (Fig. 7B). We further performed a co-IP analysis with epitope-tagged proteins in 293T cells. As expected, the Flag-labeled SIRT1 and His-labeled p66Shc co-precipitated efficiently in HEK 293T cells (Fig. 7C). These results indicated that SIRT1 interacts with p66Shc both

in bEnd.3 cells and in transiently transfected HEK-293 cells. Next, we studied which domains of SIRT1 and p66Shc contribute to the interac-tion with each other. We used Flag-labeled SIRT1 fragments and His-labeled p66Shc fragments to detect the binding region in HEK 293T cells (Fig. 7D). The C terminus of SIRT1 was found to be responsible for its interaction with p66Shc, because deletion of the C terminus completely abolished SIRT1/p66Shc interaction, whereas deletion of the N terminus did not affect their interaction (Fig. 7E). Similarly, the collagen homology (CH) 2 domain of p66Shc was responsible for its interaction with SIRT1 (Fig. 7F).

3.8. Endothelial SIRT1 decreases acetylation and phosphorylation of p66Shc

SIRT1 regulates the activity of proteins through deacetylation on lysine residues. Because SIRT1 interacts with p66Shc in bEnd.3 cells, we next investigated whether acetylation of p66Shc might be regulated by SIRT1 in endothelial cells of the spinal cord after SCI. First, we used p65, a well characterized target of SIRT1 deacetylation, to validate the acetylation activity of SIRT1 [32,33]. The increased or decreased acet-ylation levels of p65 were consistent with the diminished or elevated SIRT1 activity after knockout of SIRT1 or treatment with SRT1720 (Figs. S8A–D). Subsequently, western blotting showed that the acetyla-tion level of p66Shc was greater in SIRT1 CKO mice than SIRT1$^{fl/fl}$ mice (Fig. 8A), whereas the acetylation level of p66Shc was lower after intrathecal injection of SRT1720 than vehicle control (Figs. S9A and B). Previous studies have reported that phosphorylation of p66Shc is essential for p66Shc-mediated ROS production, and a dynamic interplay exists among post-translational modifications [34]. As expected, in parallel to acetylation, the phosphorylation of p66Shc was also elevated in SIRT1 CKO mice (Fig. 8A), whereas the phosphorylation of p66Shc decreased after intrathecal injection of SRT1720 (Figs. S9A and C). The acetylation and phosphorylation levels of p66Shc were also examined in vitro. As shown in Fig. 8B and Figs. S9D–F, treatment with IL-1β significantly increased the acetylation and phosphorylation levels of p66Shc in bEnd.3 cells. The acetylation and phosphorylation increased to a greater extent with SIRT1 knockdown (Fig. 8B); in contrast, the acetylation and phosphorylation of p66Shc significantly decreased after SIRT1 overexpression (Figs. S9D–F). Together, these results showed that endothelial SIRT1 limits the acetylation and phosphorylation of p66Shc in vitro and in vivo.
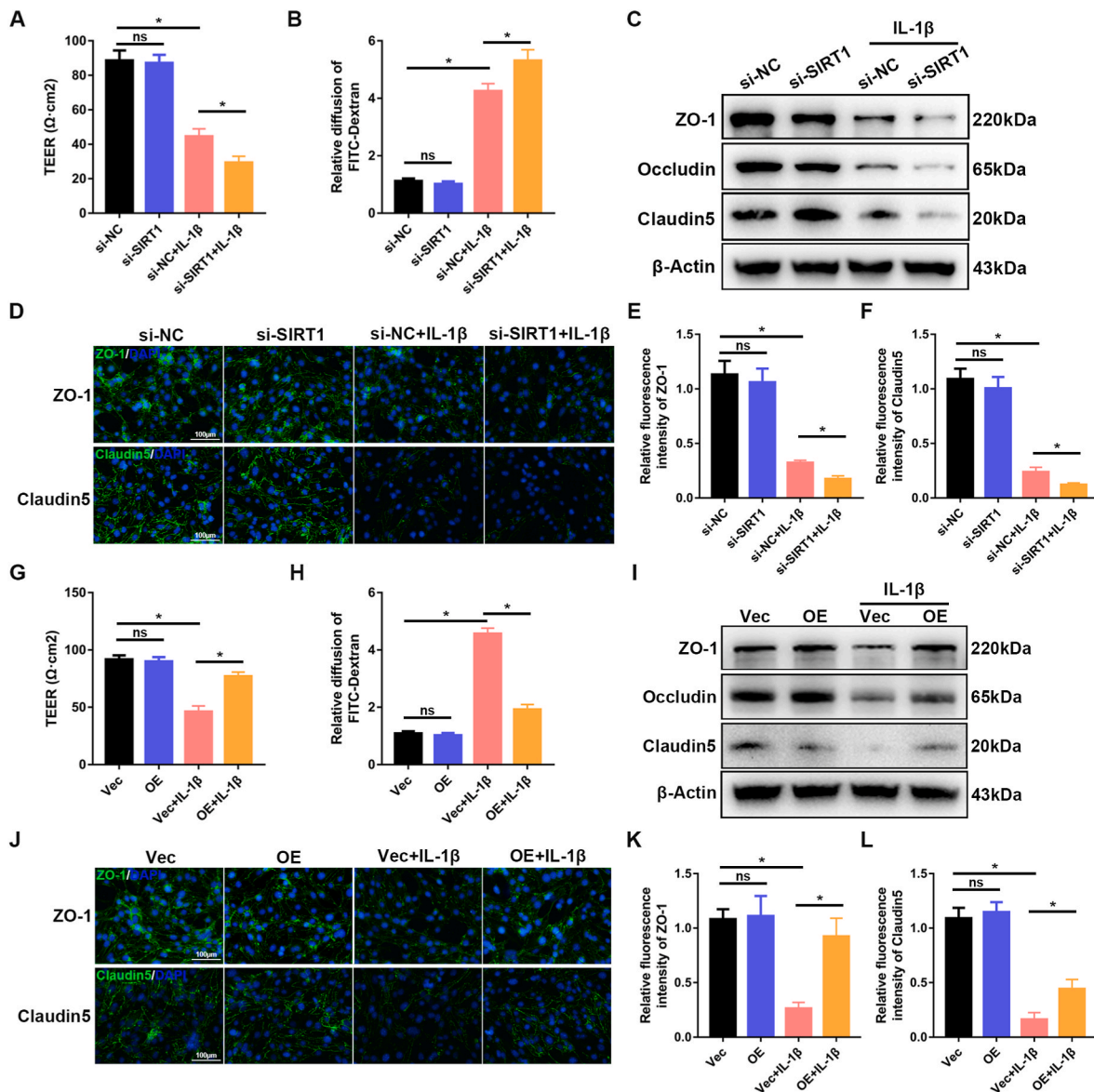
Fig. 5. SIRT1 attenuates IL-1β-induced disruption of the BSCB in vitro. bEnd.3 cells from different groups (si-NC versus si-SIRT1; Vec versus OE) were treated with or without 10 ng/ml IL-1β for 24 h. (**A, G**) TEER assays and (**B, H**) diffusion of FITC-dextran assays, conducted to evaluate the effect of SIRT1 on barrier function of bEnd.3 cells (n = 5 samples per group). Knockdown of SIRT1 exacerbated IL-1β-induced disruption of endothelial permeability, whereas overexpression of SIRT1 rescued this disruption. (**C, I**) Expression of the TJ proteins ZO-1, occludin and claudin5, evaluated by western blotting (n = 3 samples per group). Knockdown of SIRT1 significantly decreased the expression of TJ proteins, whereas overexpression of SIRT1 rescued this decrease. (**D, J**) Representative immunofluorescence images of the TJ proteins ZO-1 and claudin5 (n = 4 samples per group). (**E, F, K, L**) Quantification of the fluorescence intensity of ZO-1 and claudin5 (n = 4 samples per group). *P < 0.05; ns, not significant.

3.9. Endothelial SIRT1 attenuates oxidative stress and endothelial disruption via p66Shc

Next, we investigated whether endothelial SIRT1 might mediate the decreased ROS production and attenuation of BSCB disruption in a p66Shc-dependent manner. First, we found that SIRT1 knockdown increased ROS and decreased TJ proteins, similarly to the descriptions above, whereas p66Shc knockdown decreased ROS levels and restored TJ proteins (Fig. 8C, E-H). However, simultaneous knockdown of SIRT1 and p66Shc did not reverse the beneficial effects of p66Shc knockdown alone, thereby indicating that the increased oxidative stress caused by SIRT1 knockdown was mediated by p66Shc (Fig. 8C, E-H). Previous studies have identified lysine 81 as the target of p66Shc acetylation [34]. Subsequently, we created a p66Shc mutant that with a nonacetylatable lysine 81 (K81R). In p66ShcWT, SRIT1 overexpression decreased ROS

levels and restored TJ proteins, whereas this effect was lost in the p66ShcK81R mutant (Fig. 8D, I-L), thus, further indicating that SIRT1 regulates oxidative stress and endothelial barrier function by deacetylating p66Shc. Collectively, these results demonstrated that SIRT1 regulates oxidative stress and endothelial barrier function via p66Shc.

4. Discussion

In our study, SIRT1 was highly expressed in endothelial cells of the spinal cord, and endothelial SIRT1 was associated with BSCB function after SCI. In vivo, endothelial cell-specific knockout of SIRT1 resulted in severe disruption of the BSCB, thus resulting in widespread inflammation, neural cell death and poor functional recovery after SCI. In contrast, activation of SIRT1 by SRT1720 protected the BSCB and attenuated inflammatory cell infiltration, thereby protecting neural cells

and promoting functional recovery in mice after SCI. Through RNA-seq and IP/MS analysis, we identified p66Shc, a ROS production-associated protein, as a binding partner and potential intracellular target of SIRT1. Endothelial SIRT1 protects the BSCB after SCI by regulating oxidative

stress at least partly through deacetylation of p66Shc. We provide evidence that SIRT1 may be a promising therapeutic target for SCI (Fig. 9).

The BSCB separates the spinal cord parenchyma from the peripheral blood system and plays a crucial role in maintenance
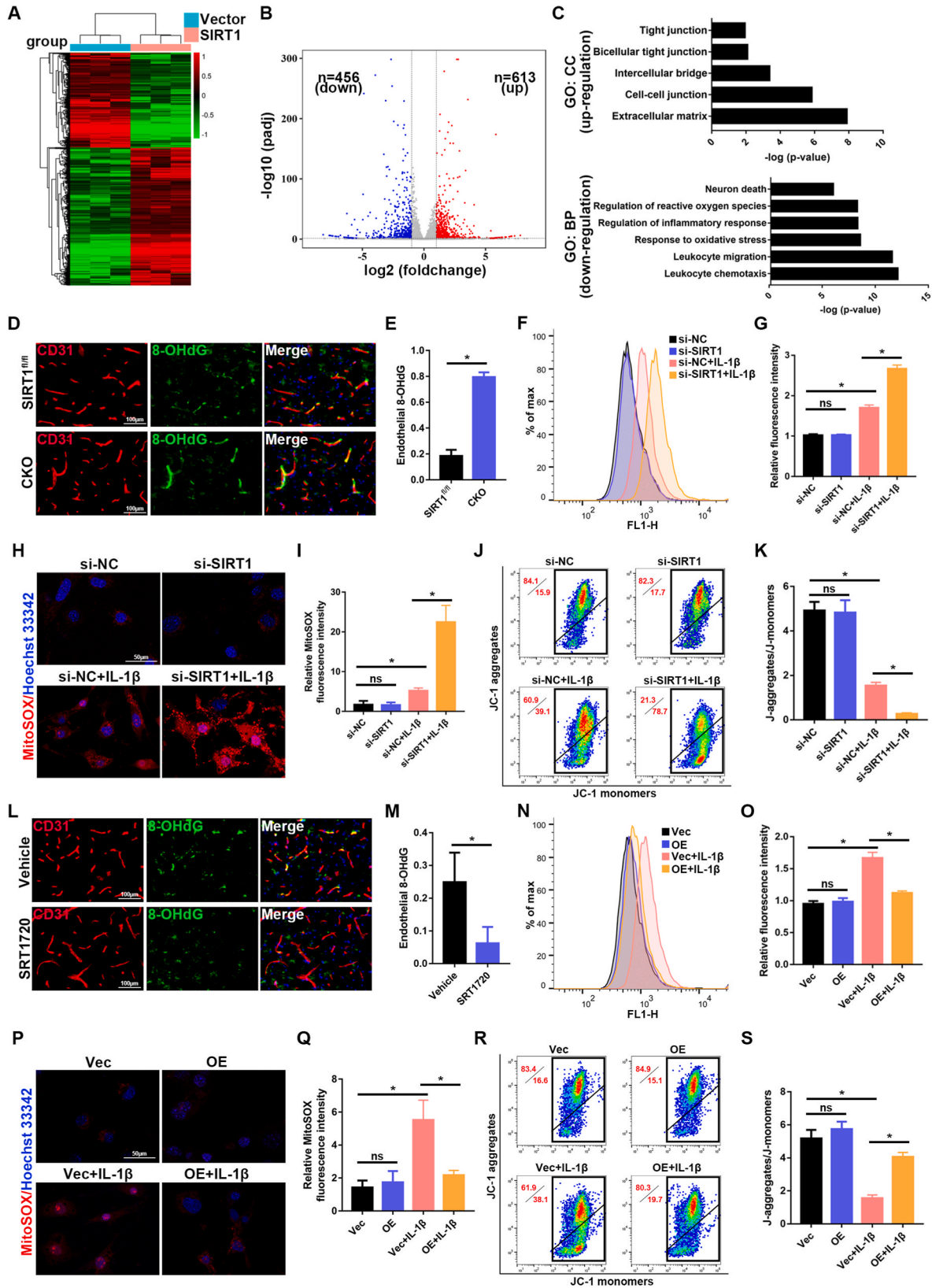
(caption on next page)

Fig. 6. Endothelial SIRT1 regulates oxidative stress. (**A**) bEnd.3 cells from different groups (vector versus SIRT1) were treated with 10 ng/ml IL-1β for 24 h, and RNA-Seq was performed. A heat map shows differentially expressed genes between vector control and SIRT1 overexpressing bEnd.3 cells in response to IL-1β. (**B**) Volcano plot of differentially expressed genes between vector control and SIRT1 overexpressing bEnd.3 cells in response to IL-1β. Red and blue dots represent up-regulated and down-regulated DEGs, respectively. (**C**) Representative up-regulated cell component (CC) and down-regulated biological pathway (BP) categories in GO analysis. (**D, L**) Representative immunofluorescence images of 8-OHdG (green) and CD31 (red) in the spinal cord at 3 d after SCI in the indicated groups (n = 6 animals per group). Sections from SIRT1 CKO mice showed significantly greater endothelial 8-OHdG than those from SIRT1$^{fl/fl}$ mice at 3 d after SCI. In contrast, the sections from SRT1720-treated mice showed significantly less endothelial 8-OHdG than vehicle control-treated mice at 3 d after SCI. (**E, M**) Quantification of endothelial 8-OHdG expression (n = 6 animals per group). (**F, N**) ROS levels of bEnd.3 cells were detected by flow cytometry in the indicated groups (n = 3 samples per group). Knockdown of SIRT1 exacerbated IL-1β-induced production of intracellular ROS, whereas overexpression of SIRT1 rescued this production. (**G, O**) Quantification of ROS levels (n = 3 samples per group). (**H, P**) Representative immunofluorescence images of MitoSOX in bEnd.3 cells in the indicated groups (n = 3 samples per group). (**I, Q**) Quantification of MitoSOX (n = 3 samples per group). (**J, R**) Mitochondrial potential of bEnd.3 cells, detected by JC-1 staining in the indicated groups (n = 3 samples per group). (**K, S**) Quantification of mitochondrial potential (n = 3 samples per group). *P < 0.05; ns, not significant. (For interpretation of the references to colour in this figure legend, the reader is referred to the Web version of this article.)

microenvironmental homeostasis in the spinal cord. However, SCI results in dramatic alterations in the microvessels and disruption of the BSCB, thus, allowing toxic serum proteins and blood-derived leukocytes to enter injury sites, and enhancing secondary injury cascades. Pathophysiological cascades develop and further contribute to dysfunction of the BSCB and to irreversible functional disabilities [2]. Noble et al. have used HRP to examine BSCB permeability after contusive SCI in rats and have reported that HRP leakage was maximal at 3 h to 1 day, whereas BSCB function was re-established by 14 days after injury [35]. Figley et al. have used EB as a marker for BSCB permeability in a clip-compression rat model of SCI and have reported that the BSCB was disrupted as early as 1 h after injury, maximum permeability was observed at 24 h postinjury, and the function of the BSCB was partially re-established by 14 days after injury [36]. In our study, we systematically examined the changes in BSCB permeability in mice after SCI induced by a dropped weight. In agreement with previous reports, our results showed that the BSCB was disrupted as early as 8 h after SCI, was

maximally disrupted at 1 d and was restored by 14 d postinjury in mice (Fig. 1A–D). We further investigated the TJs after SCI, because TJs play important roles in maintaining the function of the BBB or BSCB. The expression of TJ proteins (ZO-1, occludin and claudin5) was differentially downregulated, thus suggesting that TJs are disrupted after SCI (Fig. 1E–H). However, dysfunction in endothelial transporters (such as caveolae) or loss of specific adherens junctions (such as VE-cadherin) can also result in BSCB dysfunction [37,38] but were not further investigated in our study.

Increasing evidence suggests that SIRT1, a master regulator of energy metabolism and cellular stress, may be a therapeutic target for neurodegenerative and cerebrovascular diseases [39,40]. Recently, SIRT1 has been shown to have beneficial effects on locomotor function after SCI [41,42]. Chen et al. have reported that SIRT1 begins to decrease 4 h after SCI, is lowest at 8 h postinjury, and then is restored. Chen et al. have also used Mx1-Cre transgenic mice to delete SIRT1 in inflammatory cells and have found that SIRT1 CKO mice show exacerbated neuroinflammation
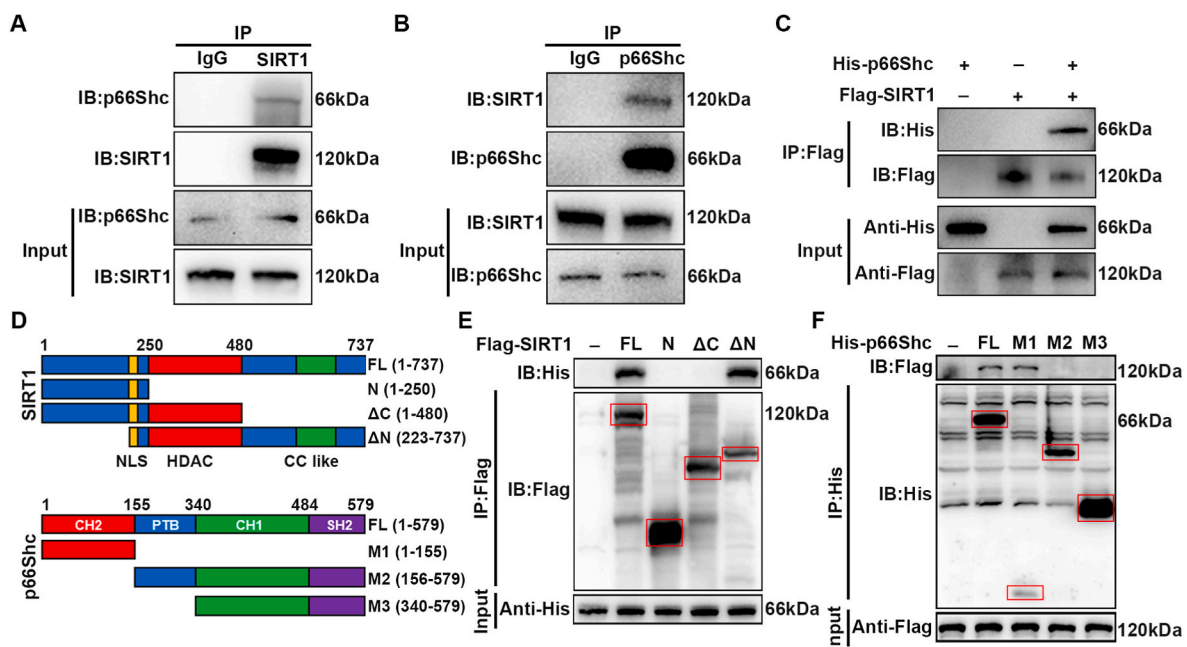
Fig. 7. SIRT1 interacts with p66Shc. (**A**) bEnd.3 cells were treated with 10 ng/ml IL-1β for 24 h, and endogenous protein interactions were assessed in whole cell lysates from bEnd.3 cells by immunoprecipitation with anti-SIRT1 or anti-IgG, and examined by immunoblotting with anti-p66Shc (n = 3 independent experiments). (**B**) bEnd.3 cells were treated with 10 ng/ml IL-1β for 24 h, and endogenous protein interactions were confirmed in whole cell lysates from bEnd.3 cells by immunoprecipitation with anti-p66Shc or anti-IgG, and examined by immunoblotting with anti-SIRT1 (n = 3 independent experiments). (**C**) Whole cell lysates from HEK 293T cells transfected with Flag-tagged SIRT1 and His-tagged p66Shc plasmids were immunoprecipitated with anti-Flag, then immunoblotted with anti-His (p66Shc) and anti-Flag (SIRT1) (n = 3 independent experiments). (**D**) Schematic diagrams of Flag-tagged full-length (FL) SIRT1, His-tagged FL p66Shc and their various deletion mutants. (**E**) HEK 293T cells were co-transfected with His-p66Shc and Flag-tagged FL SIRT1 or its deletion mutants or vectors, and whole cell lysates were assessed by immunoprecipitation followed by immunoblotting with anti-His and anti-Flag (n = 3 independent experiments). Red squares indicate immunoblots of SIRT1 fragments. (**F**) HEK 293T cells were co-transfected with Flag-SIRT1 and His-tagged FL p66Shc or its deletion mutants or vectors, and whole cell lysates were assessed by immunoprecipitation followed by immunoblotting with anti-Flag and anti-His (n = 3 independent experiments). Red squares indicate immunoblots of p66Shc fragments. (For interpretation of the references to colour in this figure legend, the reader is referred to the Web version of this article.)
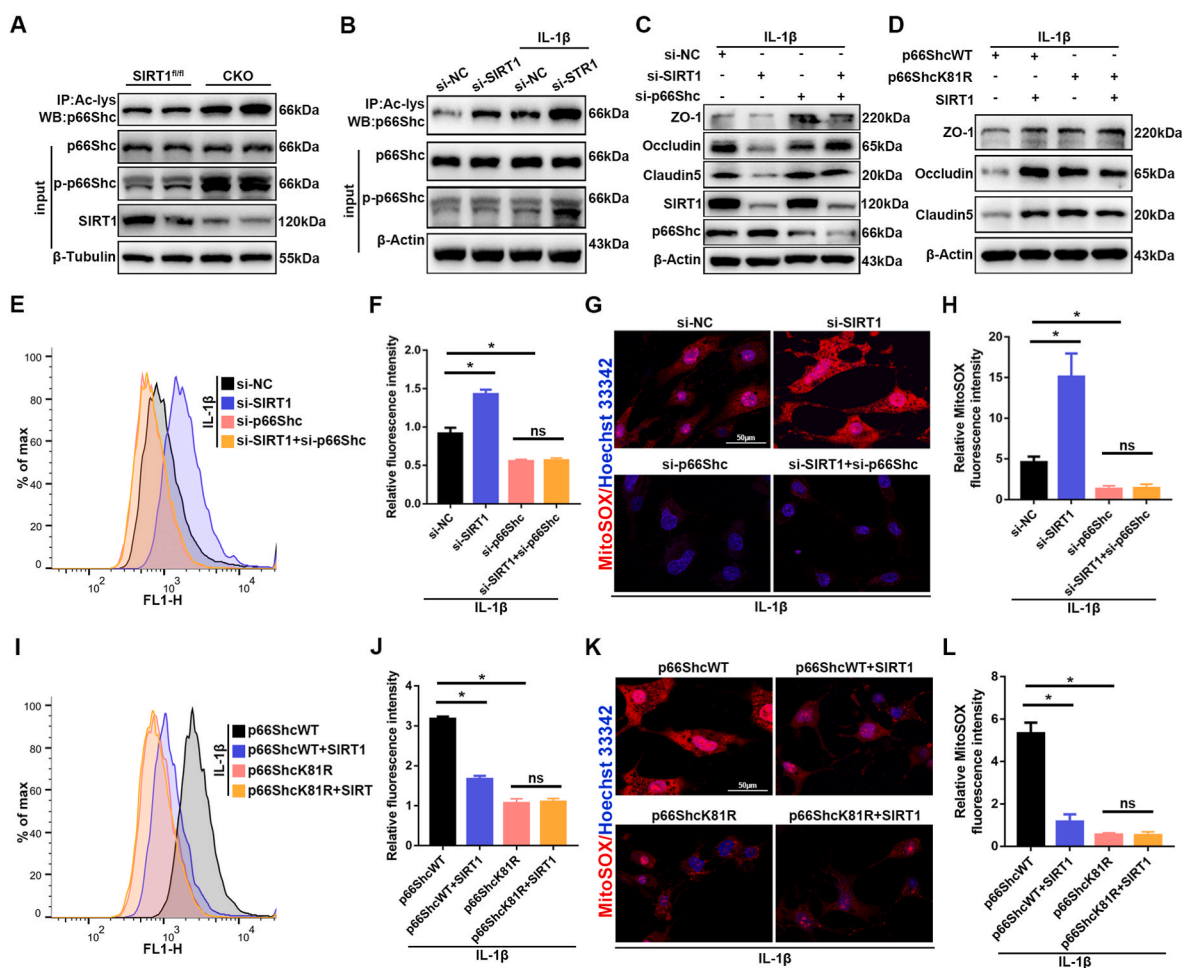
Fig. 8. Endothelial SIRT1 attenuates oxidative stress and endothelial disruption via p66Shc. (**A**) The acetylation levels of p66Shc were assessed in lysates from spinal cord tissues of SIRT1$^{fl/fl}$ and SIRT1 CKO mice at 3 d after SCI by immunoprecipitation with anti-acetyl-lysine antibody followed by immunoblotting with anti-p66Shc antibody. The phosphorylation levels of p66Shc were determined by immunoblotting with anti-p-p66Shc antibody (n = 6 animals per group). The acetylation and phosphorylation levels of p66Shc were higher in SIRT1 CKO mice than SIRT1$^{fl/fl}$ mice at 3 d after SCI. (**B**) bEnd.3 cells from different groups (si-NC versus si-SIRT1) were treated with or without 10 ng/ml IL-1β for 24 h. Western blotting analysis was used to detect changes in the acetylation and phosphorylation levels of p66Shc (n = 3 samples per group). Knockdown of SIRT1 increased the acetylation and phosphorylation levels of p66Shc. (**C**) bEnd.3 cells were transfected with si-NC or si-SIRT1 or si-p66Shc, then treated with 10 ng/ml IL-1β for 24 h. Western blotting analysis was performed to detect the expression of TJ proteins (n = 3 samples per group). (**D**) bEnd.3 cells were transfected with p66ShcWT or p66ShcK81R or SIRT1 plasmids, then treated with 10 ng/ml IL-1β for 24 h. Western blotting analysis was performed to detect the expression of TJ proteins (n = 3 samples per group). (**E, F, I, J**) Detection and quantification of ROS levels in the bEnd.3 cells in the indicated groups by flow cytometry (n = 3 samples per group). (**G, H, M, N**) Immunofluorescence detection and quantification of MitoSOX in bEnd.3 cells in the indicated groups (n = 3 samples per group). *P < 0.05; ns, not significant.

and poorer motor function than WT mice [41]. These findings are consistent with our results indicating that the expression of SITR1 significantly decreased in early stages of SCI, and then was gradually restored (Fig. 2A–C). However, a difference was observed in that the minimum levels occurred at 1 d postinjury, possibly because of the different degree of injury. To further investigate the precise role of SIRT1 after SCI, further study is necessary to clarify the specific cell types in which SIRT1 is expressed in the spinal cord. Chen et al. used immunofluorescence to show that SIRT1 is expressed in neurons (NeuN+) and macrophages/microglia (CD68+), but not in astrocytes (GFAP+) and oligodendrocytes (Olig2+) in the spinal cord in mice [41]. Another study has found that SIRT1 is distributed predominantly in neurons (NeuN+), but is absent in astrocytes (GFAP+) and microglia (Iba1+) in the spinal cord in rats [43]. However, neither study examined whether SIRT1 was expressed in microvascular endothelial cells in the spinal cord. Our results showed that SIRT1 is highly expressed in endothelial cells of the spinal cord, which are a major component of the BSCB (Fig. 2D). Based on the in vivo immunostaining and RT-PCR of isolated endothelial cells, SIRT1 expression significantly decreased in

endothelial cells of the spinal cord after SCI, thus, indicating that SIRT1 may play a crucial role in the BSCB after SCI (Fig. 2E–G). In addition, we demonstrated that endothelial cell-specific knockout of SIRT1 exacerbated disruption of the BSCB around the injury center and led to widespread inflammation, neural cell death and poor functional recovery after SCI (Fig. 3). In contrast, intrathecal injection of an SIRT1 agonist (SRT1720) protected the barrier function of the BSCB and promoted motor function recovery (Fig. 4). We further used loss- and gain-of-function experiments to confirm the protective effect of SIRT1 against IL-1β-induced endothelial barrier disruption in bEnd.3 cells in vitro (Fig. 5).

To determine the mechanism through which SIRT1 regulates BSCB function, we performed RNA-Seq and found that oxidative stress might be involved. Oxidative stress, a state in which the oxidant-antioxidant balance is disturbed, leads to ROS accumulation and plays a key role in the pathogenesis of SCI [44]. Mitochondria are the major sources of ROS production in most mammalian cells, and excessive ROS production can damage macromolecules within mitochondria, and consequently impair the electron transport chain and mitochondrial function [45].
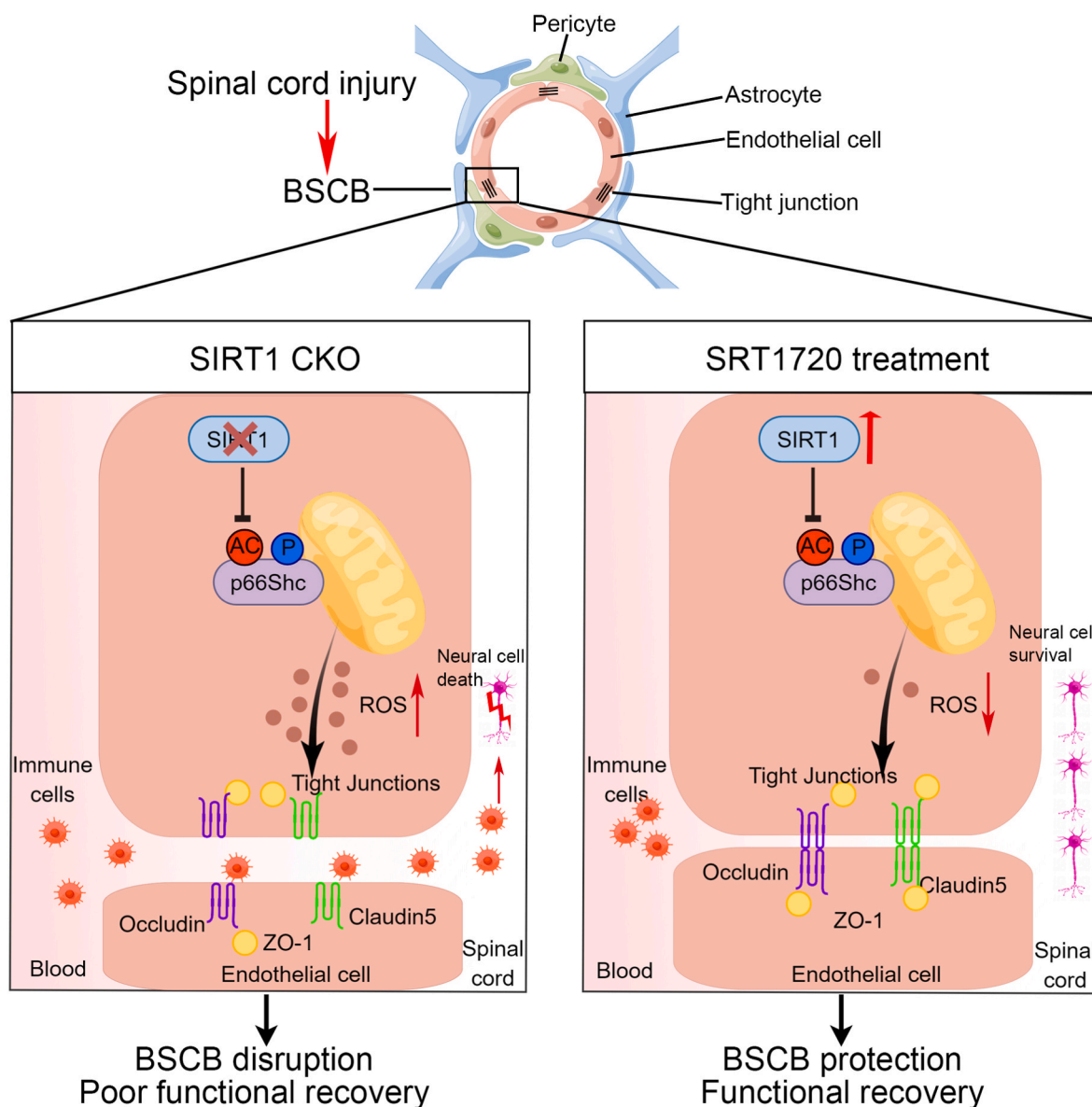
Fig. 9. SIRT1 attenuates BSCB disruption after SCI by deacetylating p66Shc. Endothelial SIRT1 decreased ROS production by limiting the acetylation and phosphorylation of p66Shc, thus attenuating BSCB disruption and inflammatory cell infiltration, protecting neural cells and promoting functional recovery in mice after SCI.

The CNS endothelial cells are particularly susceptible to oxidative stress, and numerous studies have shown that ROS can lead to BBB/BSCB dysfunction [46]. ROS affect BBB/BSCB permeability through a variety of mechanisms, including perturbation of TJ proteins [47]. Moreover, diminished ROS generation attenuates BBB/BSCB disruption, thus further supporting that oxidative stress is a crucial determinant of BBB/BSCB permeability [48]. Our results showed that SIRT1 has a protective role in BSCB function against oxidative stress after SCI (Fig. 6).

To further determine the underlying mechanism, we performed IP/MS and identified p66Shc as a putative SIRT1-interacting protein in microvascular endothelial cells. p66Shc is a redox protein belonging to the ShcA adaptor protein family, which has been reported to regulate the oxidative stress response in mammalian cells [49]. Unlike the other two ShcA isoforms p52Shc and p46Shc, in addition to containing a phospho-tyrosine binding domain, CH1 domain and sarcoma homologous type 2 domain, p66Shc contains an extra CH2 domain at N-terminus which is essential to the oxidative function of p66Shc [50]. In response to a variety of external stimuli, phosphorylation of serine 36 in the CH2 domain leads to p66Shc translocation to the mitochondria, where it oxidizes cytochrome *c* and promotes ROS production [51]. Similarly to SIRT1, p66Shc is abundantly expressed in endothelial cells, and many studies have demonstrated important roles of p66Shc in endothelial dysfunction in various diseases, including diabetes, hyperglycemia, hypertension and aging [52]. Interestingly, SIRT1 has been reported to interact with p66Shc and to decrease Ser36 phosphorylation via deacetylating p66Shc on lysine 81 in human umbilical vein endothelial cells, and SIRT1-mediated deacetylation of p66Shc has a critical role in vascular dysfunction in diabetes [34]. Our study demonstrated that p66Shc binds the C terminus of SIRT1 through the CH2 domain (Fig. 7F). The CH2 domain is positioned at the N-terminal end of p66Shc, which contains several crucial serine and threonine residues. Previous studies have suggested that the CH2 region of p66Shc can bind many proteins [53,54]. The proline-rich motif in the CH2 domain may mediate this association. After SCI, endothelial cell-specific knockout of SIRT1 increased acetylation and phosphorylation of p66Shc, thus increasing ROS production and mitochondrial dysfunction, which may be the main cause of BSCB disruption. We further demonstrated that both

knockdown of p66Shc and blocking lysine 81 acetylation by a conservative mutation to arginine decreased oxidative stress and increased TJ protein expression (Fig. 8), thus, suggesting that deacetylation of p66Shc on lysine 81 by SIRT1 may be an underlying mechanism attenuating BSCB disruption after SCI.

In conclusion, our findings suggest that endothelial SIRT1, by deacetylating p66Shc, decreases ROS production and attenuates BSCB disruption after SCI, thereby supporting the therapeutic potential of SIRT1 activators for SCI treatment.

Author Contributions

T.J., G.Y., J.C., Y.R. and S.Z. contributed to the design of the study. T.J., T.Q., P.G., Z.T., X.W., M.W., J.G., B.C., T.X., Y.H., H.L. and Z.Z. performed the experimental work and analyzed the data. T.J. wrote the main manuscript text. G.Y., J.C., Y.R. and S.Z. revised the manuscript. All authors have read and approved the manuscript.

Declaration of competing interest

All authors declare no conflicts of interest.

Data availability

Data will be made available on request.

Acknowledgements

Appendix A. Supplementary data

Supplementary data to this article can be found online at https://doi.org/10.1016/j.redox.2023.102615.

References

[1] M.V. Sofroniew, Dissecting spinal cord regeneration, Nature 557 (7705) (2018) 343–350, https://doi.org/10.1038/s41586-018-0068-4.

[2] V. Bartanusz, D. Jezova, B. Alajajian, M. Digicaylioglu, The blood-spinal cord barrier: morphology and clinical implications, Ann. Neurol. 70 (2) (2011) 194–206, https://doi.org/10.1002/ana.22421.

[3] J.Y. Lee, H.S. Kim, H.Y. Choi, T.H. Oh, T.Y. Yune, Fluoxetine inhibits matrix metalloprotease activation and prevents disruption of blood-spinal cord barrier after spinal cord injury, Brain 135 (Pt 8) (2012) 2375–2389, https://doi.org/10.1093/brain/aws171.

[4] L.Y. Jin, J. Li, K.F. Wang, W.W. Xia, Z.Q. Zhu, C.R. Wang, et al., Blood-spinal cord barrier in spinal cord injury: a Review, J. Neurotrauma 38 (9) (2021) 1203–1224, https://doi.org/10.1089/neu.2020.7413.

[5] Z. Zhao, A.R. Nelson, C. Betsholtz, B.V. Zlokovic, Establishment and dysfunction of the blood-brain barrier, Cell 163 (5) (2015) 1064–1078, https://doi.org/10.1016/j.cell.2015.10.067.

[6] H.C. Bauer, I.A. Krizbai, H. Bauer, A. Traweger, You Shall Not Pass"-tight junctions of the blood brain barrier, Front. Neurosci. 8 (2014) 392, https://doi.org/10.3389/fnins.2014.00392.

[7] N.J. Abbott, L. Ronnback, E. Hansson, Astrocyte-endothelial interactions at the blood-brain barrier, Nat. Rev. Neurosci. 7 (1) (2006) 41–53, https://doi.org/10.1038/nrn1824.

[8] S. Chang, Y. Cao, The ROCK inhibitor Y-27632 ameliorates blood-spinal cord barrier disruption by reducing tight junction protein degradation via the MYPT1-MLC2 pathway after spinal cord injury in rats, Brain Res. 1773 (2021), 147684, https://doi.org/10.1016/j.brainres.2021.147684.

[9] R.A. Frye, Phylogenetic classification of prokaryotic and eukaryotic Sir2-like proteins, Biochem. Biophys. Res. Commun. 273 (2) (2000) 793–798, https://doi.org/10.1006/bbrc.2000.3000.

[10] S. Michan, D. Sinclair, Sirtuins in mammals: insights into their biological function, Biochem. J. 404 (1) (2007) 1–13, https://doi.org/10.1042/BJ20070140.

[11] R. Menghini, V. Casagrande, M. Cardellini, E. Martelli, A. Terrinoni, F. Amati, et al., MicroRNA 217 modulates endothelial cell senescence via silent information regulator 1, Circulation 120 (15) (2009) 1524–1532, https://doi.org/10.1161/CIRCULATIONAHA.109.864629.

[12] V. Guarani, G. Deflorian, C.A. Franco, M. Kruger, L.K. Phng, K. Bentley, et al., Acetylation-dependent regulation of endothelial Notch signalling by the SIRT1 deacetylase, Nature 473 (7346) (2011) 234–238, https://doi.org/10.1038/nature09917.

[13] B. Bai, Y. Liang, C. Xu, M.Y. Lee, A. Xu, D. Wu, et al., Cyclin-dependent kinase 5-mediated hyperphosphorylation of sirtuin-1 contributes to the development of endothelial senescence and atherosclerosis, Circulation 126 (6) (2012) 729–740, https://doi.org/10.1161/CIRCULATIONAHA.112.118778.

[14] M. Potente, L. Ghaeni, D. Baldessari, R. Mostoslavsky, L. Rossig, F. Dequiedt, et al., SIRT1 controls endothelial angiogenic functions during vascular growth, Genes Dev. 21 (20) (2007) 2644–2658, https://doi.org/10.1101/gad.435107.

[15] T. Chen, S.H. Dai, X. Li, P. Luo, J. Zhu, Y.H. Wang, et al., Sirt1-Sirt3 axis regulates human blood-brain barrier permeability in response to ischemia, Redox Biol. 14 (2018) 229–236, https://doi.org/10.1016/j.redox.2017.09.016.

[16] S.M. Stamatovic, G. Martinez-Revollar, A. Hu, J. Choi, R.F. Keep, A.V. Andjelkovic, Decline in Sirtuin-1 expression and activity plays a critical role in blood-brain barrier permeability in aging, Neurobiol. Dis. 126 (2019) 105–116, https://doi.org/10.1016/j.nbd.2018.09.006.

[17] A.K. Vellimana, D.J. Aum, D. Diwan, J.V. Clarke, J.W. Nelson, M. Lawrence, et al., SIRT1 mediates hypoxic preconditioning induced attenuation of neurovascular dysfunction following subarachnoid hemorrhage, Exp. Neurol. 334 (2020), 113484, https://doi.org/10.1016/j.expneurol.2020.113484.

[18] L. Zhao, R. An, Y. Yang, X. Yang, H. Liu, L. Yue, et al., Melatonin alleviates brain injury in mice subjected to cecal ligation and puncture via attenuating inflammation, apoptosis, and oxidative stress: the role of SIRT1 signaling, J. Pineal Res. 59 (2) (2015) 230–239, https://doi.org/10.1111/jpi.12254.

[19] Y.Y. Kisanuki, R.E. Hammer, J. Miyazaki, S.C. Williams, J.A. Richardson, M. Yanagisawa, Tie2-Cre transgenic mice: a new model for endothelial cell-lineage analysis in vivo, Dev. Biol. 230 (2) (2001) 230–242, https://doi.org/10.1006/dbio.2000.0106.

[20] A. Fantin, J.M. Vieira, A. Plein, L. Denti, M. Fruttiger, J.W. Pollard, et al., NRP1 acts cell autonomously in endothelium to promote tip cell function during sprouting angiogenesis, Blood 121 (12) (2013) 2352–2362, https://doi.org/10.1182/blood-2012-05-424713.

[21] F.Q. Kong, S.J. Zhao, P. Sun, H. Liu, J. Jie, T. Xu, et al., Macrophage MSR1 promotes the formation of foamy macrophage and neuronal apoptosis after spinal cord injury, J. Neuroinflammation 17 (1) (2020) 62, https://doi.org/10.1186/s12974-020-01735-2.

[22] E.E. Crouch, F. Doetsch, FACS isolation of endothelial cells and pericytes from mouse brain microregions, Nat. Protoc. 13 (4) (2018) 738–751, https://doi.org/10.1038/nprot.2017.158.

[23] X. Ge, P. Tang, Y. Rong, D. Jiang, X. Lu, C. Ji, et al., Exosomal miR-155 from M1-polarized macrophages promotes EndoMT and impairs mitochondrial function via activating NF-kappaB signaling pathway in vascular endothelial cells after traumatic spinal cord injury, Redox Biol. 41 (2021), 101932, https://doi.org/10.1016/j.redox.2021.101932.

[24] H. Shi, H.L. Wang, H.J. Pu, Y.J. Shi, J. Zhang, W.T. Zhang, et al., Ethyl pyruvate protects against blood-brain barrier damage and improves long-term neurological outcomes in a rat model of traumatic brain injury, CNS Neurosci. Ther. 21 (4) (2015) 374–384, https://doi.org/10.1111/cns.12366.

[25] Y. Rong, W. Liu, J. Wang, J. Fan, Y. Luo, L. Li, et al., Neural stem cell-derived small extracellular vesicles attenuate apoptosis and neuroinflammation after traumatic spinal cord injury by activating autophagy, Cell Death Dis. 10 (5) (2019) 340, https://doi.org/10.1038/s41419-019-1571-8.

[26] C.J. Czupalla, S. Liebner, K. Devraj, Vitro models of the blood-brain barrier, Methods Mol. Biol. 1135 (2014) 415–437, https://doi.org/10.1007/978-1-4939-0320-7_34.

[27] S. Hu, Y. Wu, B. Zhao, H. Hu, B. Zhu, Z. Sun, et al., Panax notoginseng saponins protect cerebral microvascular endothelial cells against oxygen-glucose deprivation/reperfusion-induced barrier dysfunction via activation of PI3K/Akt/Nrf2 antioxidant signaling pathway, Molecules 23 (11) (2018), https://doi.org/10.3390/molecules23112781.

[28] K.D. Beck, H.X. Nguyen, M.D. Galvan, D.L. Salazar, T.M. Woodruff, A.J. Anderson, Quantitative analysis of cellular inflammation after traumatic spinal cord injury: evidence for a multiphasic inflammatory response in the acute to chronic environment, Brain 133 (Pt 2) (2010) 433–447, https://doi.org/10.1093/brain/awp322.

[29] J.C. Fleming, M.D. Norenberg, D.A. Ramsay, G.A. Dekaban, A.E. Marcillo, A.D. Saenz, et al., The cellular inflammatory response in human spinal cords after injury, Brain 129 (Pt 12) (2006) 3249–3269, https://doi.org/10.1093/brain/awl296.

[30] L. Wu, S.H. Ramirez, A.M. Andrews, W. Leung, K. Itoh, J. Wu, et al., Neuregulin1-beta decreases interleukin-1beta-induced RhoA activation, myosin light chain phosphorylation, and endothelial hyperpermeability, J. Neurochem. 136 (2) (2016) 250–257, https://doi.org/10.1111/jnc.13374.

[31] I.A. Krizbai, H. Bauer, N. Bresgen, P.M. Eckl, A. Farkas, E. Szatmari, et al., Effect of oxidative stress on the junctional proteins of cultured cerebral endothelial cells, Cell. Mol. Neurobiol. 25 (1) (2005) 129–139, https://doi.org/10.1007/s10571-004-1378-7.

[32] F. Yeung, J.E. Hoberg, C.S. Ramsey, M.D. Keller, D.R. Jones, R.A. Frye, et al., Modulation of NF-kappaB-dependent transcription and cell survival by the SIRT1 deacetylase, EMBO J. 23 (12) (2004) 2369–2380, https://doi.org/10.1038/sj.emboj.7600244.

[33] F. Ghisays, C.S. Brace, S.M. Yackly, H.J. Kwon, K.F. Mills, E. Kashentseva, et al., The N-terminal domain of SIRT1 is a positive regulator of endogenous SIRT1-

dependent deacetylation and transcriptional outputs, Cell Rep. 10 (10) (2015) 1665–1673, https://doi.org/10.1016/j.celrep.2015.02.036.

[34] S. Kumar, Y.R. Kim, A. Vikram, A. Naqvi, Q. Li, M. Kassan, et al., Sirtuin1-regulated lysine acetylation of p66Shc governs diabetes-induced vascular oxidative stress and endothelial dysfunction, Proc. Natl. Acad. Sci. U. S. A. 114 (7) (2017) 1714–1719, https://doi.org/10.1073/pnas.1614112114.

[35] L.J. Noble, J.R. Wrathall, Distribution and time course of protein extravasation in the rat spinal cord after contusive injury, Brain Res. 482 (1) (1989) 57–66, https://doi.org/10.1016/0006-8993(89)90542-8.

[36] S.A. Figley, R. Khosravi, J.M. Legasto, Y.F. Tseng, M.G. Fehlings, Characterization of vascular disruption and blood-spinal cord barrier permeability following traumatic spinal cord injury, J. Neurotrauma 31 (6) (2014) 541–552, https://doi.org/10.1089/neu.2013.3034.

[37] M.D. Sweeney, Z. Zhao, A. Montagne, A.R. Nelson, B.V. Zlokovic, Blood-brain barrier: from physiology to disease and back, Physiol. Rev. 99 (1) (2019) 21–78, https://doi.org/10.1152/physrev.00050.2017.

[38] M. Oudega, Molecular and cellular mechanisms underlying the role of blood vessels in spinal cord injury and repair, Cell Tissue Res. 349 (1) (2012) 269–288, https://doi.org/10.1007/s00441-012-1440-6.

[39] F. Zhang, S. Wang, L. Gan, P.S. Vosler, Y. Gao, M.J. Zigmond, et al., Protective effects and mechanisms of sirtuins in the nervous system, Prog. Neurobiol. 95 (3) (2011) 373–395, https://doi.org/10.1016/j.pneurobio.2011.09.001.

[40] Y. Horio, T. Hayashi, A. Kuno, R. Kunimoto, Cellular and molecular effects of sirtuins in health and disease, Clin. Sci. (Lond.) 121 (5) (2011) 191–203, https://doi.org/10.1042/CS20100587.

[41] H. Chen, H. Ji, M. Zhang, Z. Liu, L. Lao, C. Deng, et al., An agonist of the protective factor SIRT1 improves functional recovery and promotes neuronal survival by attenuating inflammation after spinal cord injury, J. Neurosci. 37 (11) (2017) 2916–2930, https://doi.org/10.1523/JNEUROSCI.3046-16.2017.

[42] X. Feng, X. Chen, M. Zaeem, W. Zhang, L. Song, L. Chen, et al., Sesamol attenuates neuroinflammation by regulating the AMPK/SIRT1/NF-kappaB signaling pathway after spinal cord injury in mice, Oxid. Med. Cell. Longev. 2022 (2022), 8010670, https://doi.org/10.1155/2022/8010670.

[43] Q. Yin, J.F. Wang, X.H. Xu, H. Xie, Effect of lycopene on pain facilitation and the SIRT1/mTOR pathway in the dorsal horn of burn injury rats, Eur. J. Pharmacol. 889 (2020), 173365, https://doi.org/10.1016/j.ejphar.2020.173365.

[44] Z.S. Ji, G.B. Gao, Y.M. Ma, J.X. Luo, G.W. Zhang, H. Yang, et al., Highly bioactive iridium metal-complex alleviates spinal cord injury via ROS scavenging and inflammation reduction, Biomaterials 284 (2022), 121481, https://doi.org/10.1016/j.biomaterials.2022.121481.

[45] C. Guo, L. Sun, X. Chen, D. Zhang, Oxidative stress, mitochondrial damage and neurodegenerative diseases, Neural Regen. Res. 8 (21) (2013) 2003–2014, https://doi.org/10.3969/j.issn.1673-5374.2013.21.009.

[46] P.B. Pun, J. Lu, S. Moochhala, Involvement of ROS in BBB dysfunction, Free Radic. Res. 43 (4) (2009) 348–364, https://doi.org/10.1080/10715760902751902.

[47] G. Schreibelt, G. Kooij, A. Reijerkerk, R. van Doorn, S.I. Gringhuis, S. van der Pol, et al., Reactive oxygen species alter brain endothelial tight junction dynamics via RhoA, PI3 kinase, and PKB signaling, FASEB J. 21 (13) (2007) 3666–3676, https://doi.org/10.1096/fj.07-8329com.

[48] Y.S. Jung, S.W. Lee, J.H. Park, H.B. Seo, B.T. Choi, H.K. Shin, Electroacupuncture preconditioning reduces ROS generation with NOX4 down-regulation and ameliorates blood-brain barrier disruption after ischemic stroke, J. Biomed. Sci. 23 (2016) 32, https://doi.org/10.1186/s12929-016-0249-0.

[49] E. Migliaccio, M. Giorgio, S. Mele, G. Pelicci, P. Reboldi, P.P. Pandolfi, et al., The p66shc adaptor protein controls oxidative stress response and life span in mammals, Nature 402 (6759) (1999) 309–313, https://doi.org/10.1038/46311.

[50] H.A. Mir, R. Ali, U. Mushtaq, F.A. Khanday, Structure-functional implications of longevity protein p66Shc in health and disease, Ageing Res. Rev. 63 (2020), 101139, https://doi.org/10.1016/j.arr.2020.101139.

[51] M. Giorgio, E. Migliaccio, F. Orsini, D. Paolucci, M. Moroni, C. Contursi, et al., Electron transfer between cytochrome c and p66Shc generates reactive oxygen species that trigger mitochondrial apoptosis, Cell 122 (2) (2005) 221–233, https://doi.org/10.1016/j.cell.2005.05.011.

[52] S. Kumar, P66Shc and vascular endothelial function, Biosci. Rep. 39 (4) (2019), https://doi.org/10.1042/BSR20182134.

[53] G. Xi, X. Shen, D.R. Clemmons, p66shc inhibits insulin-like growth factor-I signaling via direct binding to Src through its polyproline and Src homology 2 domains, resulting in impairment of Src kinase activation, J. Biol. Chem. 285 (10) (2010) 6937–6951, https://doi.org/10.1074/jbc.M109.069872.

[54] F.A. Khanday, L. Santhanam, K. Kasuno, T. Yamamori, A. Naqvi, J. Dericco, et al., Sos-mediated activation of rac1 by p66shc, J. Cell Biol. 172 (6) (2006) 817–822, https://doi.org/10.1083/jcb.200506001.